CERN-TH.7413/94
WUB 94-24
hep-lat/9409005
August 1994

Observing Long Colour Flux Tubes in SU(2) Lattice Gauge Theory[1]

G.S. Bali[b], K. Schilling[a,b], Ch. Schlichter[b][2]

[a] *CERN, Theory Division, CH-1211 Geneva-23, Suisse*
[b] *Physics Department, University of Wuppertal, D-42097 Wuppertal, Germany*

Abstract

We present results of a high statistics study of the chromo field distribution between static quarks in $SU(2)$ gauge theory on lattices of volumes 16^4, 32^4, and $48^3 \times 64$, with physical extent ranging from 1.3 fm up to 2.7 fm at $\beta = 2.5$, $\beta = 2.635$, and $\beta = 2.74$. We establish string formation over physical distances as large as 2 fm. The results are tested against Michael's sum rules. A detailed investigation of the transverse action and energy flux tube profiles is provided. As a by-product, we obtain the static lattice potential in unpreceded accuracy.

(extended version)
September 7, 1994

---

[1] Work supported in part by DFG grant Schi 257/3-2 and EC contract CHRX-CT92-00551.

[2] Email: bali/schillin/schlicht@wpts0.physik.uni-wuppertal.de

1 Introduction

The issue of verifying the confinement mechanism in Quantum Chromodynamics has been a great challenge ever since the phenomenon of string formation between a static $Q\bar{Q}$ pair has been conceived by t'Hooft and Mandelstam [1] to be a dual Meissner effect in the scenario of a Type II superconducting vacuum. Early lattice gauge theory attempts to compute the colour field distribution, without recourse to modelling, were necessarily limited by the available compute power and lattice methods of the period. They rendered qualitative rather than quantitative results, with lattice resolutions, a, and quark-antiquark separations, r, restrained to $a > .15$ fm and $r = aR < 1$ fm, respectively [2, 3, 4, 5].

In recent high precision studies of $SU(2)$ and $SU(3)$ gauge theories [6, 7] the static quark-antiquark potential has been found to be consistent with a linearly rising part and a subleading $-\pi/(12R)$ correction as predicted by the bosonic string picture [8, 9] for separations above $r_t \approx .5$ fm. Moreover, there are numerical indications for hybrid potentials, with gluonic excitations separated by energy gaps $n\pi/R$ [10, 11] as expected from effective string theories [8].

A compelling evidence about the nature of the confining string from lattice gauge theory (LGT) is still lacking. It would require measurements of field distributions at quark separations well beyond r_t. To study the geometry of the colour flux tube between Q and $\bar{Q}$ sources, one needs an increase both in *resolution* of the underlying lattice and in the *linear extent*, r, of the string.

These requirements are not so easily met, since (a) the energy density carries dimension a^{-4} and therefore imposes a lower limit onto the lattice spacing due to statistical noise and (b) one is forced to work with very large lattices to attain large quark-antiquark separations $r = Ra$. On top of this, one is of course faced with the ubiquitous problem of filtering ground state signals out of an excited state background.

Thus, in order to really determine the structure of strings in the heavy quark-antiquark interaction, one cannot avoid a systematic high precision study, ensuring (a) good scaling behaviour as well as (b) sufficient control on finite size effects (FSE) and (c) reliable signals for the ground state.

The superconducting picture for QCD has been modelled in terms of a dual effective Langrangian some time ago by Baker and collaborators and worked out subsequently [12]. Lattice gauge theory in principle offers the laboratory to test such confinement models, as it allows for *ab initio* studies from the QCD Lagrangian. Within the lattice community, there has recently been revived interest to study the rôle of monopole condensation in the confinement mechanism, by recourse to the maximal Abelian gauge projection, in $SU(2)$ gauge theory [13, 14, 15]. Some first encouraging evidence for the dual Meissner effect has also been reported [16]. Nevertheless, all this pioneering lattice work on the confinement mechanism has been carried out either at rather smallish quark-antiquark separations, where the flux tube is not yet really developed, or at rather large lattice spacing.

In fact, there definitely remains a gap: so far flux tubes of sufficient physical lengths have never been observed on the lattice! In this paper, we intend to bridge this gap: exploiting state-of-the-art lattice techniques — for noise reduction and ground state enhancement — as well as the compute power (and memory!) of "small" Connection Machines CM-2 and CM-5, we will be able to demonstrate unambiguously that quenched $SU(2)$ gauge theory does imply flux tube formation over distances well above the π Compton wavelength.

Reliable lattice calculations can only be based on trustworthy error estimates. For this reason, we will expose the underlying lattice techniques in quite some detail (Section 2). There is a shorter Section 3, augmented by three appendices, on (a) weak coupling and (b) string model issues that are helpful to appreciate certain qualitative features of the field distributions and (c) sum rules for energy and action densities that provide an important cross check of the lattice results. The numerical results are presented in Section 4 which includes very precise potential data, determination of the Symanzik β function and many pictures of the flux tubes[3]. Detailed checks on finite size effects, discretization effects and ground state dominance are provided, substantiating the interpretation of lattice correlators in terms of continuum fields. Section 5 contains a discussion of the shape of the flux tube and the status of Michael's sum rules.

2 Lattice techniques

The numerical calculations are performed on lattices with hypercubic geometry and periodic boundary conditions in all four directions with volumes $L_S^3 \times L_T$ ranging from 16^4 up to $48^3 \times 64$. Throughout the simulation the standard Wilson action

$$S_W = -\beta \sum_{n,\mu>\nu} U_{\mu\nu}(n) \qquad (1)$$

with

$$U_{\mu\nu}(n) = \frac{1}{2}\mathrm{Tr}\left(U_\mu(n)U_\nu(n+\hat{\mu})U_\mu^\dagger(n+\hat{\nu})U_\nu^\dagger(n)\right) \qquad (2)$$

and $\beta = 4/g^2$ has been used.

For the updating of the gauge fields a hybrid of heatbath and overrelaxation algorithms has been implemented [17]. The Fabricius-Haan heatbath sweeps [18] have

---

[3] We regret being unable to expose the colour flux tube in colour in this medium! A data base of colour images is under construction. It can be accessed via anonymous ftp from wpts0.physik.uni-wuppertal.de. The (compressed) .rgb and .ps files are deposited in the directory pub/colorflux.

been randomly mixed with the overrelaxation step with probability ranging from 1/8 at $\beta = 2.5$ up to 1/14 at $\beta = 2.74$. The links have been visited in lexicographical ordering within 2^4 hypercubes, i.e. within each such hypercube, first all links pointing into direction $\hat{1}$ are visited site by site, then all links in direction $\hat{2}$ etc..

2.1 Prerequisites

In order to substantiate continuum results from lattice calculations it is of utmost importance to investigate the impact of the finite lattice volume as well as the scaling behaviour with the lattice spacing a. This requires simulations both at (a) fixed lattice coupling β (i.e. spacing a) with a varying number of lattice sites and (b) (approximately) fixed physical volume but different lattice resolutions.

Of course one wants to work — within the computational means — as close as possible to the continuum limit, i.e. at as large β-values as possible. The bottleneck is set by the memory requirements due to the increase of the number of lattice sites (needed to compensate for a smaller a) as well as by the computer time required to suppress the statistical noise. Since the operators under investigation scale with the fourth power of the lattice resolution (up to $\ln a$ terms from anomalous dimensions, see below), the latter limitation is the more serious one, restricting all preceding lattice studies to $\beta \leq 2.5$.

Though simulations at small β values allow for rather large physical volumes, lattice artefacts are expected to spoil results at physically interesting scales. Moreover, we should mention that our smearing procedure provides inferior ground state overlaps at large lattice spacings. There is more reason to stay away from too coarse lattices: one needs a sufficiently large T-range for verification of T-plateaus in the *bona fide* physical quantities. In addition, at smaller values of β, the lower limit $T \geq 3$, implied by the minimal temporal extent of the $\langle \Box \rangle_{\mathcal{W}}$ operator, amounts to overly large physical separations and leads to small signals of the Wilson loops.

In short, one has to find a way between Scylla and Charybdis: i.e. to compromise between the shortcomings of both small and large lattice spacings a. We have chosen to simulate at $\beta = 2.5, 2.635$, and 2.74 at various lattice volumes, ranging up to the unpreceded volume $48^3 \times 64$. Our simulation parameters are summarized in Tab. 1.

As a by-product we compute the static potential and obtain the most precise set of $SU(2)$ string tension values that has ever been computed on the lattice. Details of the fitting procedure are explained in Section 4.1.2. The (lattice) string tension K relates the lattice spacing a to a physical scale: $\kappa = Ka^2$. We ascribe the "canonical" value $\sqrt{\kappa} = 440$ MeV to the square root of the string tension. Needless to say that this scale, taken from real world QCD Regge trajectories, only serves as an orientation for

	$\beta = 2.50$	$\beta = 2.50$	$\beta = 2.635$	$\beta = 2.74$
$L_S^3 \times L_T$	16^4	32^4	$48^3 \times 64$	32^4
K	.0350(4)	.0350(12)	.01458(8)	.00830(6)
a/fm	.0826(5)	.0826(14)	.0541(2)	.0408(2)
a^{-1}/GeV	2.35 (1)	2.35(4)	3.64(1)	4.83(2)
aL_S/fm	1.32(1)	2.64(4)	2.60(1)	1.31(1)
MC sweeps	868000	255600	53800	152000
thermalization sweeps	2000	51000	4200	4000
meas., sweeps between meas.				
Wilson loops	8680, 100	2046, 100	248, 200	1480, 100
colour flux distribution	8680, 100	2046, 100	248, 200	670, 100
plaquette	86800, 10	20460, 10	992, 50	14800, 10

Table 1: *Simulation parameters. The physical scales have been computed from the value* $\sqrt{K}a = 440$ *MeV.*

its poor man's quenched two colour version: $SU(2)$ gauge theory. Nonetheless, the quantitative agreement between the $SU(2)$ and $SU(3)$ potentials is remarkable. We also point out that the effective string model with which we are going to compare our results does not depend on the underlying gauge group.

From the string tension measurement we find the following (approximate) relation between the present lattice spacings: $a_{2.5}^{-1} : a_{2.635}^{-1} : a_{2.74}^{-1} \approx 1 : 1.5 : 2$. Thus, the 16^4 lattice at $\beta = 2.5$ has approximately the same physical volume as the 32^4 lattice at $\beta = 2.74$. The same holds true for the 32^4 lattice at $\beta = 2.5$ and the $48^3 \times 64$ lattice at $\beta = 2.635$. These pairs of lattices can be used to investigate the a (in)dependence of the results. In order to reveal possible volume effects, the 16^4 and 32^4 lattice outcomes at $\beta = 2.5$ will be compared with each other.

As a prerequisite to the present investigation, let us consider the static $Q\bar{Q}$ potential which can be computed from Wilson loops, $W(R,T)$. A Wilson loop, i.e. an ordered product of link variables along a closed rectangular path with spatial separation R and temporal extent T, can be interpreted as a world sheet of a $Q\bar{Q}$ pair: at Euclidean time $\tau = 0$ a creation operator

$$\Gamma_R^\dagger = Q(0)U(0 \to R)Q^\dagger(R) \tag{3}$$

with a gauge covariant transporter $U(0 \to R)$ is applied to the vacuum state $|0\rangle$. The $Q\bar{Q}$ pair is then propagated to $\tau = T$ by static Wilson lines in presence of the gauge field background, and finally annihilated by application of Γ_R. A spectral decomposition of the Wilson loop exhibits the following behaviour ($\mathcal{T} = \rceil^{-\dashv\mathcal{H}}$ denotes the transfer matrix, $\mathcal{T}|n\rangle = e^{-E_n}|n\rangle$):

$$\langle W(R,T)\rangle \quad = \quad \frac{\mathrm{Tr}\left(\Gamma_R \mathcal{T}^T \Gamma_R^\dagger \mathcal{T}^{L_T - T}\right)}{\mathrm{Tr}\left(\mathcal{T}^{L_T}\right)}$$

$$\begin{aligned} &= \frac{1}{\sum_m e^{-E_m L_T}} \sum_{m,n} |\langle m|\Gamma_R|n,R\rangle|^2\, e^{-V_n(R)T} e^{-E_m(L_T-T)} && (4)\\ &= \sum_n |d_n(R)|^2 e^{-V_n(R)T} \times \left(1+\mathcal{O}\left(e^{-E_1(L_T-T)}\right)\right) \quad , \end{aligned}$$

where $d_n(R) = \langle 0|\Gamma_R|n,R\rangle$. $|n,R\rangle$ is the nth eigenstate in the charged sector of the Hilbert space with non-vanishing overlap to the creation operator $\Gamma_R^\dagger$, while $|n\rangle$ is the nth eigenstate of the zero charge sector. $V_n(R)$ denotes the nth excitation of the $Q\bar{Q}$ potential and the vacuum energy E_0 has been set to *zero*. E_1 is the mass gap, i.e. the mass of the A_1^+ glueball.

Actually, we are not restricted to on-axis $Q\bar{Q}$ separations, $\mathbf{R} = (\mathbf{R},\mathbf{0},\mathbf{0})$. Planar Wilson loops can be easily generalized to off-axis separations by connecting sources that do not share a common lattice axis. In the present investigation, the following off-axis directions have been realized:

$$\begin{aligned} \mathbf{d}_1 &= (1,0,0) \quad , \quad \mathbf{d}_2 = (1,1,0) \quad , \quad \mathbf{d}_3 = (2,1,0) \quad , \\ \mathbf{d}_4 &= (1,1,1) \quad , \quad \mathbf{d}_5 = (2,1,1) \quad , \quad \mathbf{d}_6 = (2,2,1) \quad , \end{aligned} \tag{5}$$

with separations $m_i\mathbf{d}_i$ up to $m_1, m_2, m_4 \leq L_S/2$ and $m_3, m_5, m_6 \leq L_S/4$. For the largest lattice, $L_S = 48$, this amounts to a measurement over a set of 108 different separations. All paths have been chosen as close to the shortest linear connection between the sources as the lattice permitted.

2.2 Noise reduction

In this section we will shortly discuss the implications of noise reduction that we achieved by integrating out the temporal links in the Wilson loops analytically [19].

The link integration amounts to the following substitution:

$$U_4(n) \longrightarrow V_4(n) = \frac{\int_{SU(2)} dU\, U e^{\beta S_{n,4}(U)}}{\int_{SU(2)} dU\, e^{\beta S_{n,4}(U)}} \tag{6}$$

with

$$S_{n,\mu}(U) = \frac{1}{2}\mathrm{Tr}\left(U F_\mu^\dagger(n)\right) \quad , \quad F_\mu(n) = \sum_{\nu\neq\mu} U_\nu(n) U_\mu(n+\hat{\nu}) U_\nu^\dagger(n+\hat{\mu}) \quad . \tag{7}$$

$V_4(n)$ is in general not an $SU(2)$ element anymore.

In this way, time-like links are replaced by the mean field value they take in the neighbourhood of (stroboscopically frozen) links that interact through the staples $F_\mu(n)$.

Only those links that do not share a common plaquette, can be integrated independently. This holds in particular for all temporal links within our spatially smeared Wilson loops, iff $R > 1$.

In case of $SU(2)$ gauge theory, $V_4(n)$ can be calculated analytically:

$$V_4(n) = \frac{I_2(\beta f_\mu(n))}{f_\mu(n) I_1(\beta f_\mu(n))} F_\mu(n) \quad , \quad f_\mu(n) = \sqrt{\det(F_\mu(n))} \quad . \tag{8}$$

I_n denote the modified Bessel functions.

The statistical error, ΔO, of an observable, $\langle O \rangle$, calculated *without* link integration, is related by a constant $s < 1$ to the corresponding error *with* link integration, $\Delta O_{li} = s\Delta O$. In order to discuss the impact of link integration on noise reduction, we start from the naïve expectation that each integrated link contributes equally to s, i.e. we assume $s = x^{2T}$ with $2T$ being the number of integrated links used within the construction of $\langle O \rangle$.

In order to estimate the value of s, let us consider on-axis Wilson loops with integrated temporal links. On symmetric lattices ($L_T = L_S$) we expect from the relation $\langle W(R,T) \rangle = \langle W(T,R) \rangle$:

$$\frac{\Delta W(R,T)}{\Delta W(T,R)} = x^{2(T-R)} \quad . \tag{9}$$

This leads to the estimate for x^2:

$$x^2 = \exp\left(\frac{1}{T-R} \log\left(\frac{\Delta W(R,T)}{\Delta W(T,R)}\right)\right) \quad . \tag{10}$$

Our data (with bootstrapped errors of the errors) is consistent with a factor[4] $x = .889 \pm .001$ ($x = .890 \pm .001$) for $\beta = 2.5$ ($\beta = 2.635$). Thus, application of link integration at time $T = 6$ (the largest temporal extent, used in the computation of the colour field operators, see below) amounts to a reduction of computer time by a factor $x^{-24} = 16.8 \pm 0.4$.

The improvement achieved by link integration tends to be smaller at smaller lattice spacings. This is due to the fact that the physical extent of the neighbourhood to be integrated out becomes smaller. On the other hand, the error of a non-link integrated operator, measured on lattices with constant physical volumes but different couplings, also decreases with the lattice spacing (temperature β^{-1}). At the bottom line, the two effects almost cancel each other and the relative errors of link integrated Wilson loops appear to remain rather independent of the lattice resolution, provided that the physical lattice volumes and the number of measurements are kept constant.

---

[4] For small R and T where the statistical errors have reached the same order of magnitude as the numerical machine accuracy, we performed additional computations of ΔO and ΔO_{li} on smaller subsamples to ensure that the errors still follow the statistical $1/\sqrt{N_{meas}}$ expectation.

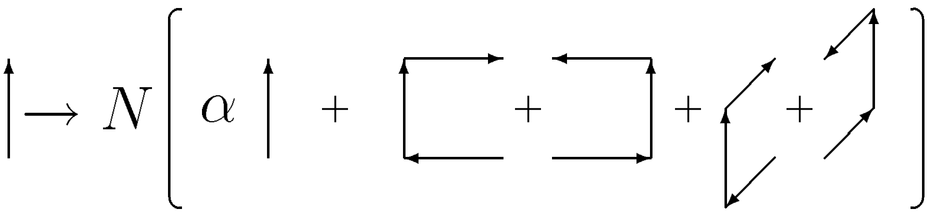

Figure 1: *Visualization of a smearing iteration.*

2.3 Ground state enhancement

The physically interesting ground state potential, $V(R) = V_0(R)$, can be retrieved in the limit of large T:

$$\langle W(R,T)\rangle = \sum_n C_n(R) e^{-V_n(R)T} \longrightarrow C_0(R) e^{-V(R)T} \quad (T \to \infty) \quad . \tag{11}$$

The overlaps $C_n(R) = |d_n(R)|^2 \geq 0$ obey the following normalization condition:

$$\sum_n C_n(R) = 1 \quad . \tag{12}$$

The path of the transporter $U(0 \to R)$ used for the construction of the $Q\bar{Q}$ creation operator (Eq. 3) does not affect the eigenvalues of the transfer matrix and is by no means unique. One can exploit this freedom to maximize the ground state overlap by a suitable superposition of such paths, aiming at $C_0(R) \approx 1$. At any given value of R, the final deviation of $C_0(R)$ from *one* can serve as a monitor for the suppression of excited state contributions actually achieved in this way.

In the present simulation an iterative procedure (with n_{iter} iteration steps) has been applied [20, 21]: each *spatial* link $U_i(n)$, occurring in the transporter, is substituted by a "fat" link,

$$U_i(n) \longrightarrow N\left(\alpha U_i(n) + \sum_{j\neq i} U_j(n) U_i(n+\hat{j}) U_j^\dagger(n+\hat{i})\right) \tag{13}$$

with the appropriate normalization constant N and free parameter α. One such iteration step is visualized in Fig. 1. For this smearing, the links are visited in the lexicographical ordering of the updating sweep.

We find satisfactory ground state enhancement with the parameter choice $n_{iter} = 150$ and $\alpha = 2$.

One can define approximants to the asymptotic potential values and overlaps, $V(R,T) \to V(R)$ and $C_0(R,T) \to C_0(R)$ $(T \to \infty)$. Due to the positivity of the transfer matrix

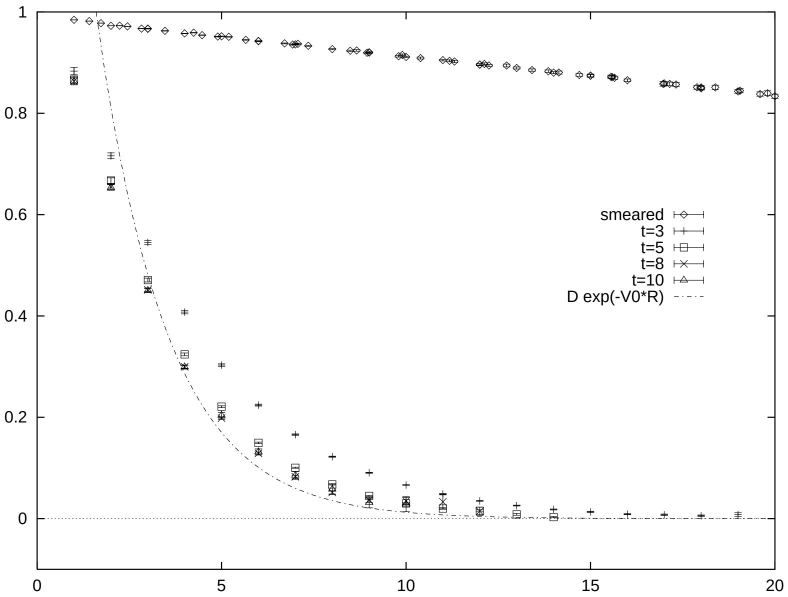

Figure 2: *The ground state overlaps $C_0(R)$ versus R at $\beta = 2.635$. In addition to the overlaps of smeared operators (diamonds), finite T approximants, $C_0(R,T)$ for the overlaps from unsmeared (on-axis) operators are plotted. The dashed line denotes the extrapolated large T limit for the unsmeared overlaps and should be a valid approximation to the large R behaviour.*

T, these quantities decrease monotonically (in T) to their asymptotic limits:

$$V(R,T) = \log\left(\frac{\langle W(R,T)\rangle}{\langle W(R,T+1)\rangle}\right) = V(R) + \frac{C_1(R)}{C_0(R)}h(R,T) + \cdots \qquad (14)$$

$$C_0(R,T) = \frac{\langle W(R,T)\rangle^{T+1}}{\langle W(R,T+1)\rangle^{T}} = C_0(R) + C_1(R)h(R,T) + \cdots \qquad (15)$$

with

$$h(R,T) = e^{-\Delta V(R)T}\left(1 - e^{-\Delta V(R)}\right) \quad , \quad \Delta V(R) = V_1(R) - V(R) \quad . \qquad (16)$$

In our analysis, we follow these approximants until they reach a plateau.

As we wish to maximize $C_0(R)$, we would like to acquire a qualitative understanding of the underlying physics. For this purpose, we consider unsmeared on-axis Wilson loops. Combining Eq. 11 with the R-T symmetry[5] $\langle W(R,T)\rangle = \langle W(T,R)\rangle$ and the parametrization of the potential $V(R) = V_0 - e/R + KR$ we obtain

$$\begin{aligned} \ln\langle W(R,T)\rangle &\approx \ln C_0(R,T) - V_0T + eT/R - KRT \\ &= \ln D - V_0(R+T) + e(R/T + T/R) - KRT \end{aligned} \qquad (17)$$

---

[5] This symmetry is only exact on lattices with $L_S = L_T$. However, within statistical accuracy it also holds true on the $48^3 \times 64$ lattice.

for large R and T and arrive at the estimate (with constants V_0 and e obtained from the potential analysis below),

$$C_0(R,T) = De^{-(V_0-e/T)R} \quad \text{or} \quad C_0(R) = De^{-V_0R} \quad . \tag{18}$$

This parametrization of the unsmeared overlaps turns out to describe the off-axis data too if we allow for a smaller (direction dependent) constant V_0.

The self-energy term V_0/a diverges in the continuum limit, $a \to 0$. Thus, the overlaps at fixed physical separation[6], $r = Ra$, decrease with increasing β. This feature is in accord with the following consideration: in the scaling region the transverse size of the $Q\bar{Q}$ wave function is expected to remain constant in physical units while the transverse extent of the string like creation operator remains on the scale of the lattice resolution. Thus, the ground state overlap of this operator decreases with increasing correlation length.

The ground state overlaps of smeared Wilson loops at $\beta = 2.635$ are shown in Fig. 2, together with on-axis approximants to the unsmeared overlaps and the asymptotic (large R) estimate of Eq. 18 (dashed curve), where the coefficient $D \approx 2.3$ was obtained by fitting the large T data to Eq. 18. There is obviously a dramatic improvement from the use of an extended creation operator. In case of the smeared links, the (unsmeared) self-energy contribution V_0 appears to be reduced to a number $f \ll V_0$ that is sufficiently small to allow for an expansion of the exponential factor $C_0(R) = D\exp(-fR) \approx D(1-fR)$: the ground state overlaps of smeared Wilson loops exhibit a *linear* R dependence throughout the observed R region. Moreover, rotational invariance in terms of the overlaps is restored for all on- and off-axis separations.

For $\beta = 2.5$ the overlaps vary between $C_0(\sqrt{2}a) = .95$ and $C_0(r_m) = .73$ on the 32^4 lattice and from $C_0(a) = .98$ to $C_0(r_m) = .81$ on the 16^4 lattice. Within the same physical region the $\beta = 2.635$ overlaps range from $C_0(\sqrt{2}a) = .98$ to $C_0(r_m) = .81$. At $\beta = 2.74$ we have used an inferior set of smearing parameters ($n_{iter} = 40$ and $\alpha = 0$); yet we achieve overlaps of $C_0(a) = .96$ and $C(r_m) = .84$. We have chosen $r_m \approx 1.2$ fm for the comparison. This scale corresponds to $r_m a^{-1} = 8\sqrt{3}, 12\sqrt{3}, 16\sqrt{3}$ for the three β-values, respectively. Even at fixed physical r the overlaps tend to increase with β, unlike in the situation with unsmeared operators: the wave function becomes smoother at increased correlation length and can be better modelled by the iterative smearing procedure. For the largest distance realized (2.25 fm at $\beta = 2.635$) we still achieve the value $C_0(24\sqrt{3}a) = .72$.

The success of smearing is twofold: (a) for rather small values of T, extraction of the ground state potential becomes possible and (b) the signal-to-noise ratio is greatly improved as $C_0(R)$ (and the signal) increases, especially for large values of R.

---

[6] At fixed (lattice) R, a (slight) increase is observed and expected.

2.4 Lattice determination of colour fields

The central observables in our present investigation are the action and energy densities in presence of two static quark sources (with separation R) in the ground state of the binding problem:

$$\epsilon_R(\mathbf{n}) = \frac{1}{2}\left(\mathcal{E}_R(\mathbf{n}) + \mathcal{B}_R(\mathbf{n})\right) \quad , \tag{19}$$

$$\sigma_R(\mathbf{n}) = \frac{1}{2}\left(\mathcal{E}_R(\mathbf{n}) - \mathcal{B}_R(\mathbf{n})\right) \quad , \tag{20}$$

with

$$\mathcal{E}_R(\mathbf{n}) = \langle \mathbf{E}^2(\mathbf{n})\rangle_{|0,R\rangle - |0\rangle} \quad , \quad \mathcal{B}_R(\mathbf{n}) = \langle \mathbf{B}^2(\mathbf{n})\rangle_{|0,R\rangle - |0\rangle} \tag{21}$$

and

$$\langle O\rangle_{|0,R\rangle - |0\rangle} = \langle 0,R|O|0,R\rangle - \langle 0|O|0\rangle \quad . \tag{22}$$

The sign convention corresponds to the Minkowski notation with metric $\eta = \mathrm{diag}(1,-1,-1,-1)$, in which $\mathcal{B}_R(\mathbf{n}) \leq 0$, $\mathcal{E}_R(\mathbf{n}) \geq 0$. We point out that the Minkowski action density carries a different sign relative to the (negative) Euclidean action, i.e. $S_W = -\sum_{\mathbf{n}} \frac{1}{2}\langle \mathbf{E}^2 - \mathbf{B}^2\rangle_{|0\rangle}$.

We shall extract these observables from the correlations between smeared Wilson loops, $\mathcal{W} = W(R,T)$, and (unsmeared) plaquettes $\Box(\tau) = U_{\mu\nu}(\mathbf{n},\tau)$ (Eq. 2)[7],

$$\langle \Box(S)\rangle_{\mathcal{W}} = \frac{1}{2}\frac{\langle \mathcal{W}(\Box(T/2+S) + \Box(T/2-S))\rangle}{\langle \mathcal{W}\rangle} - \langle \Box\rangle \quad . \tag{23}$$

S denotes the distance of the plaquette from the central time slice of the Wilson loop and takes the values $S = 0, 1, \ldots$ ($S = 1/2, 3/2, \ldots$) for even (odd) T.

The plaquette insertion acts as the chromo dynamical analogue of a Hall detector in electrodynamics[8]. For $0 \leq S < T/2$, $\langle \Box(S)\rangle_{\mathcal{W}}$ can be decomposed into mass eigenstates as follows

$$\langle \Box(S)\rangle_{\mathcal{W}} = \frac{\mathrm{Tr}\left(\Gamma\left(\mathcal{T}^{T/2+S}\Box\mathcal{T}^{T/2-S} + \mathcal{T}^{T/2-S}\Box\mathcal{T}^{T/2+S}\right)\Gamma^\dagger\mathcal{T}^{L_T-T}\right)}{2\mathrm{Tr}\left(\Gamma\mathcal{T}^T\Gamma^\dagger\mathcal{T}^{L_T-T}\right)} - \langle \Box\rangle$$

---

[7] We do not follow the authors of Ref. [4] who, in order to reduce statistical fluctuations, advocate to subtract $\langle \mathcal{W}\Box(\mathbf{n})\rangle/\langle \mathcal{W}\rangle$ with the reference point, $\mathbf{n}$, taken far away from the sources rather than the vacuum plaquette expectation $\langle \Box\rangle$. In this way, we avoid possible shifts of the normalization relative to the vacuum energy and action densities. We would like to point out that we found no reduction in statistical errors for smeared Wilson loop operators by using the above suggestion. However, we have been able to confirm this observation of Ref. [4] for unsmeared Wilson loops.

[8] We note in passing, that the authors of Ref. [22] have chosen to connect the plaquette to the Wilson loop via two Wilson lines and take one overall trace instead of two separate ones, as this leads to an improved signal to noise ratio. However, a prove that this observable indeed can be interpreted as a colour field density in presence of a static $Q\bar{Q}$ pair is missing. Moreover, the constraint through sum rules is lost.

$$
\begin{aligned}
&= \langle 0,R|\Box|0,R\rangle - \langle 0|\Box|0\rangle \\
&+ 2\mathrm{Re}\left(\frac{d_1}{d_0}\langle 1,R|\Box|0,R\rangle\right) e^{-\Delta V T/2}\cosh(\Delta V S) \\
&+ \frac{|d_1|^2}{|d_0|^2}\left(\langle 1,R|\Box|1,R\rangle - \langle 0,R|\Box|0,R\rangle\right) e^{-\Delta V T} \\
&+ 2\mathrm{Re}\left(\frac{d_2}{d_0}\langle 2,R|\Box|0,R\rangle\right) e^{-(V_2-V)T/2}\cosh((V_2-V)S) \\
&+ \mathcal{O}(e^{-\Delta V(\frac{3}{2}T-S)}) \quad .
\end{aligned}
\tag{24}
$$

ΔV denotes the gap between the ground state and the first excitation (Eq. 16). In principle, $|d_n|^2 = C_n(R)$ and $V_n(R)$ can be determined from smeared Wilson loops. The non-diagonal $\mathcal{O}(e^{-(V_n-V)(T/2-S)})$ coefficients can only be obtained from a fit to the time dependence of the above operator. As we shall see in the next paragraph, $(V_2-V)/2 \approx \Delta V$. Thus, a measurement of the excited state colour field distribution $\langle\Box\rangle_{|1,R\rangle-|0\rangle}$ appears to be unfeasible with the present method.

In string model calculations the separations between ground and excited state potentials without gluonic angular momentum, i.e. within the A_{1g} representation of the cubic symmetry group, are found to be multiples of $2\pi/R$ [8, 10]. This feature is in accord with numerical simulations of $SU(2)$ and $SU(3)$ gauge theories [10, 11]. Therefore, as a net result, we expect the following asymptotic behaviour:

$$
\begin{aligned}
\langle\Box(S)\rangle_{\mathcal{W}} &= \langle\Box\rangle_{|0,R\rangle-|0\rangle} \\
&+ c_1 e^{-\pi T/R}\cosh(2\pi S/R) \\
&+ c_2 e^{-2\pi T/R}\left(1 + c_3\cosh(4\pi S/R)\right) + \cdots
\end{aligned}
\tag{25}
$$

with c_i being free parameters. They are, contrary to the coefficients of the spectral decomposition of the Wilson loop (Eq. 11), not necessarily positive! Be aware, that c_i vary with the $Q\bar{Q}$ separation as well as with the spatial position $\mathbf{n}$ of the plaquette insertion.

The deviations from the asymptotic values are governed by $\mathcal{O}(e^{-\Delta V(T/2-S)})$ terms, compared to order $e^{-\Delta V T}$ corrections in case of the potential (Eqs. 14, 16). So, the issue of optimization for ground state dominance is certainly more critical for field measurements. While the reduction of systematic errors would ask for large T-values, the suppression of statistical uncertainties would lead one to the contrary. Obviously, the reasonable strategy is to ensure that systematic and statistical errors are kept in balance.

A weak coupling expansion of the plaquette yields the square of the Maxwell field strength tensor $\mathcal{F}_{\mu\nu} = F^c_{\mu\nu}\sigma_c/2$:

$$
U_{\mu\nu} = 1 - \frac{a^4}{2\beta}F^c_{\mu\nu}F^c_{\mu\nu} + \mathcal{O}(a^6) \quad . \tag{26}
$$

Thus, by an appropriate choice of $\Box = U_{i4}$ ($\Box = U_{jk}$) expectation values of squared chromo electric (magnetic) field components can be obtained[9], in the limit of large T:

$$\frac{2\beta}{a^4}\langle U_{i4}(S)\rangle_W \quad \overset{T\to\infty}{\longrightarrow} \quad \langle E_i^2(\mathbf{n})\rangle_{|0,R\rangle - |0\rangle} \quad , \tag{27}$$

$$-\frac{2\beta}{a^4}\langle U_{jk}(S)\rangle_W \quad \overset{T\to\infty}{\longrightarrow} \quad \langle B_i^2(\mathbf{n})\rangle_{|0,R\rangle - |0\rangle} \quad , \quad |\epsilon_{ijk}| = 1 \quad . \tag{28}$$

The finite T corrections to these relations have been elaborated in Eq. 25. Note, that $E_i^2 = E_i^c E_i^c = 2\mathrm{Tr}E_i^2$.

2.5 Implementation of colour field operators

For measurement of the colour field distributions, the appropriate plaquette operators are suitably averaged in order to obtain chromo magnetic or electric insertions in symmetric position to a given lattice site, $\mathbf{n}$. For the electric insertions two plaquettes are averaged:

$$U_{i4}(\mathbf{n}) \to \frac{1}{2}\left(U_{i4}(\mathbf{n}-\mathbf{e}_i) + U_{i4}(\mathbf{n})\right) \quad . \tag{29}$$

For the magnetic fields four adjacent plaquettes are combined:

$$U_{jk}(\mathbf{n}) \to \frac{1}{4}\left(U_{jk}(\mathbf{n}-\mathbf{e}_j-\mathbf{e}_k) + U_{jk}(\mathbf{n}-\mathbf{e}_j) + U_{jk}(\mathbf{n}-\mathbf{e}_k) + U_{jk}(\mathbf{n})\right) \quad . \tag{30}$$

Notice that while B_i^2 is measured at integer values of τ, E_i^2 is measured between two time slices. To minimize contaminations from excited states (Eq. 25), τ is chosen as close as possible to $T/2$. For even temporal extent of the Wilson loop, this means $S = 0$ for the magnetic field operator and $S = 1/2$ for the electric field insertion, while for odd T, $S = 0(1/2)$ for electric (magnetic) fields.

For measurement of the colour field distributions we have restricted ourselves to on-axis separations of the two sources. All even distances $R = 2, 4, \ldots, R_{\max}$ with $R_{\max} = 8, 24, 36$ for $L_S = 16, 32, 48$, respectively, have been realized. In order to identify the asymptotic plateau, T was varied up to[10] $T = 6$. The colour field distributions have been measured up to a transverse distance $n_\perp = 2$ along the entire $Q\bar{Q}$ axis. In between the two sources and up to 2 lattice spacings outside the sources, the transverse distance was increased to $n_{\perp,\max} = 6, 10, 15$ for the three lattice extents $L_S = 16, 32, 48$, respectively. In addition to "on-axis" positions, $\mathbf{n} = (n_1, n_2, 0)$, we chose plane-diagonal points $\mathbf{n} = (n_1, n_2, n_2)$ with $n_2 < n_{\perp,\max}/\sqrt{2}$. We averaged

---

[9] Remember, that we do not obtain any information on the components of $\mathbf{E}$ and $\mathbf{B}$ themselves since, in general, $\langle O^2\rangle \neq \langle O\rangle^2$.

[10] For historical reasons, on our small lattice volumes (16^4 at $\beta = 2.5$ and 32^4 at $\beta = 2.74$) only the odd values $T = 1, 3, 5, 7$ have been realized.

over various coordinates $\mathbf{n}$, exploiting the cylindrical and reflection symmetry of the problem. All this amounts to 9576 (26244) different combinations of R, T, and $\mathbf{n}$ on the 32^4 ($48^3 \times 64$) lattices, on which both $\langle U_{jk}\rangle_{\mathcal{W}}$ and $\langle U_{i4}\rangle_{\mathcal{W}}$ have been computed.

The temporal parts of the Wilson loops, appearing in the colour field correlator, have been link integrated. Therefore, the electric components have only been determined at distances larger than one lattice spacing away from the sources. For the case of the 32^4 lattice at $\beta = 2.5$ we have substituted the missing values by the corresponding entries, computed on a 16^4 lattice without link integration. Distances so close to the sources are not relevant to continuum physics anyway, due to contamination from the heavy quark self-energy and lattice artefacts.

3 Theoretical expectations

3.1 Perturbative scenario

A perturbative order g^4 computation of the lattice potential can be found in Ref. [23]. Here, we recall the one gluon exchange result only:

$$V(\mathbf{R}) = -C_F g^2 \left(G_L(\mathbf{R}) - G_L(\mathbf{0})\right) \overset{a\to 0}{\longrightarrow} -C_F g^2 \frac{1}{4\pi R} \tag{31}$$

where we have dropped the (divergent) self energy in the continuum expression. The lattice gluon propagator $G_L(\mathbf{R})$ (Eqs. 78, 77) can be computed numerically on finite lattices. For $SU(2)$ one has $C_F = (N^2-1)/(2N) = 3/4$. For completeness, this expression is derived in Appendix A. A renormalization of the bare lattice coupling $g^2 = 2N/\beta$ turns out to be the main effect of the loop diagrams that occur in the next order.

In order to investigate the nature of lattice artefacts, we have performed a weak coupling expansion of the action and energy densities. The lowest order term is a two gluon exchange. To this order the action and energy densities turn out to identical, both receiving just contributions from electric plaquettes. Details of the calculation are contained in Appendix A. The lattice integrals of the result (Eqs. 83, 84) have been computed numerically.

In the continuum limit one finds the expression (from Eq. 90),

$$\epsilon_R^{(c)}(0, n_\perp) = g^2 C_F \frac{1}{(4\pi)^2} \frac{R^2}{\left(R^2/4 + n_\perp^2\right)^3} \quad , \tag{32}$$

for the energy density distribution in the central transverse plane. In Figs. 3 and 4 we present a comparison of the dipole fields on finite (32^3) and infinite lattices with their

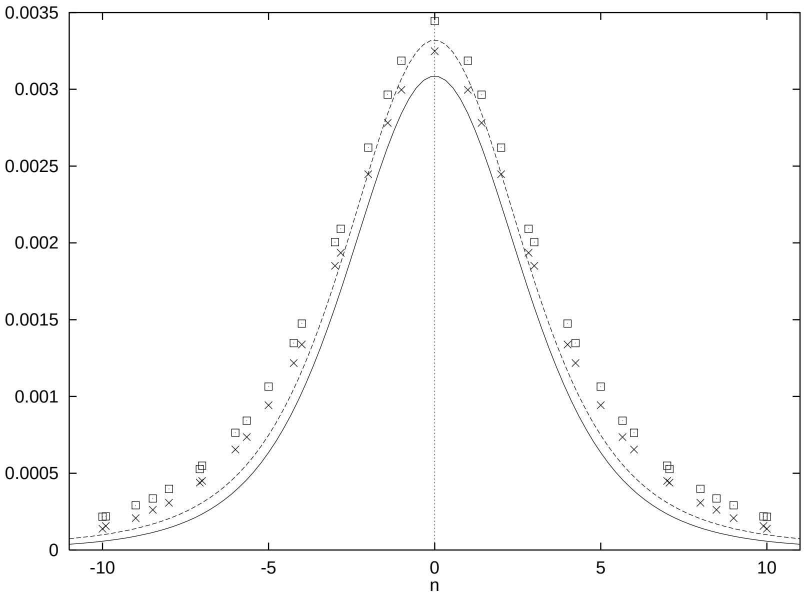

Figure 3: *Comparison between continuum and lattice dipole fields in the center plane between two sources, separated by* $R = 12$. *The ordinate,* n, *is the distance from the* $Q\bar{Q}$ *axis. The values have been multiplied by a factor* $(4\pi)^2/(C_F g^2)$. *Crosses and the solid line correspond to the infinite volume results. Squares and the dashed line are obtained at finite volume,* $R/L_S = 12/32$.

continuum forms[11], for separations $R = 12$ and $R = 4$, respectively. The field positions are chosen both along a transverse lattice axis and a plane-diagonal (multiples of $\sqrt{2}$).

Up to order g^4 corrections, perturbative lattice and continuum calculations equally lead to[12]

$$\sum_{\mathbf{n}} a^3 \sigma_R(\mathbf{n}) \approx \sum_{\mathbf{n}} a^3 \epsilon_R(\mathbf{n}) \approx \frac{V(R)}{a} \quad . \tag{33}$$

As argued in the appendix, perturbation theory is expected to describe the energy density better than the action density.

3.2 Nonperturbative expectation

In the limit of large $Q\bar{Q}$ separations, i.e. if the width of the flux tube becomes small relative to its length, an effective relativistic string model is expected to describe the

---

[11] The continuum formula on a finite lattice has been elaborated in Appendix D.

[12] To obtain the continuum expression, $\sum_{\mathbf{n}} a^3$ simply has to be replaced by $\int d^3x$.

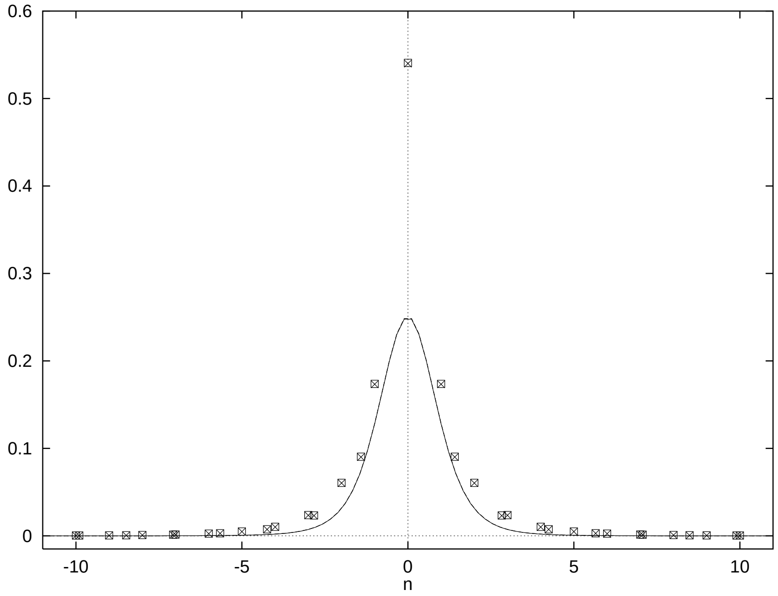

Figure 4: *Same as Fig. 3 for* $R = 4$.

infra red aspects of the interaction. Classical solutions of such string Lagrangians predict, in agreement with the strong coupling expectation of pure gauge theory, an area law of Wilson loops and, thus, a linearly rising long range contribution to the potential. However, in reality, a quantum mechanical string will fluctuate. An ultra violet cut-off has to be imposed on the wave length of such fluctuations, beyond which longitudinal degrees of freedom become important and the (non renormalizable) string theory looses its applicability. For a huge class of string models the string fluctuations lead to a universal subleading Coulomb type contribution [8], $-(d-2)\pi/(24R)$, to the potential in the Gaussian approximation (d denotes the number of space-time dimensions). For large R, excitations are expected to be separated from the ground state by multiples of π/R [8].

The leading order expectation of string models for correlators of smooth, large Wilson loops, $\mathcal{W}$ and $\Box$ with boundaries $\partial\mathcal{W}$ and $\partial\Box$ is

$$\langle \mathcal{W}\Box\rangle - \langle\mathcal{W}\rangle\langle\Box\rangle \propto \exp\left(-KA(\partial\mathcal{W},\partial\Box)\right) \quad , \tag{34}$$

where $A(\partial\mathcal{W},\partial\Box)$ is the minimal area of a surface with boundary $\partial\mathcal{W}\cup\partial\Box$ and K is the string tension. Approximating the Wilson loop and the plaquette by circles, the authors of Ref. [24] obtained in the limit $n_\perp \ll R$

$$\langle E_1^2\rangle \propto \exp\left(-\frac{K\pi}{\ln R}n_\perp^2\right) \quad . \tag{35}$$

Thus, the central width of the fluctuating string

$$\delta^2_{\epsilon_R} = \langle n^2_\perp \rangle_{\epsilon_R} = \frac{\int dn_\perp \, n^3_\perp \epsilon_R(0, n_\perp)}{\int dn_\perp \, n_\perp \epsilon_R(0, n_\perp)} \tag{36}$$

is expected to diverge logarithmically with the quark separation:

$$\delta^2_{\epsilon_R} = \delta^2_0 \ln \frac{R}{R_0} \quad , \tag{37}$$

where R_0 is an ultra violet cut-off parameter. In a quantum mechanical calculation, this relation has been confirmed in the Gaussian approximation for the probability of the fluctuating string, crossing the central transverse plane $n_1 = 0$ at the position $n_\perp$ [24].

For small distances, the perturbative result of Eq. 32 suggests a linear divergence of the width:

$$\delta^2_{\epsilon_R} = \frac{R^2}{4} \quad . \tag{38}$$

For $n_\perp \ll R$ (and large r) where the string picture is applicable a Gaussian transverse profile of the flux tube is expected. At large $n_\perp$, however, correlators of (unsmeared) Wilson loops with plaquettes can be viewed as glueball correlation functions in rotated space-time. Thus, for $n_\perp \gg R, T$ an exponential form, governed by the mass gap, might be expected[13].

3.3 Sum rules

Some important consistency conditions, relating the local chromo field operators to the global $Q\bar{Q}$ potential have been derived by Michael [25]. In the following we will shortly recall these sum rules. More details and comments related to contaminations from excited states can be found in Appendices B and C.

The action sum rule relates the action to the derivative of the potential with respect to the inverse coupling

$$\begin{aligned} \sum_{\mathbf{n}} a^3 \sigma_R(\mathbf{n}) &= -\frac{1}{a}\frac{\partial V(R)}{\partial \ln \beta} && (39) \\ &= -\frac{\partial \ln a}{\partial \ln \beta} v(R) - \frac{1}{a}\frac{\partial V_0}{\partial \ln \beta} \quad , && (40) \end{aligned}$$

---

[13] However, the wave function of the $Q\bar{Q}$ pair, created at $\tau = 0$ has to be decayed into its ground state, before the colour fields are measured at $\tau = T/2$. Due to the structure of the action, a Hamiltonian evolution in the strong coupling limit only allows hopping between neighbouring sites. Thus, in this limit, communication occurs only between sites within the light cone $n_\perp < T/2$ and the limit $n_\perp \gg T$ is not justified. As illustrated by the above example, the exponential decay prediction for large $n_\perp$ has to be taken with care.

where we have decomposed the potential $V(R) = av(R) + V_0$ into a physical part, $v(R)$, that remains constant as $a \to 0$, and a diverging self energy contribution, V_0. The action sum rule is an exact relation. It is in accord with the perturbative expectation Eq. 33, which follows by inserting the leading order expression for $V(R)$ (Eq. 31) into Eq. 39.

The energy sum rule involves derivatives with respect to anisotropic spatial and temporal couplings. After relating the latter to the isotropic lattice coupling, β, via a weak coupling series, one ends up with an approximate sum rule. Thus, unlike the action sum rule, the energy sum rule is not exact on the lattice. Here, we just state the leading order expectation

$$\sum_{\mathbf{n}} a^3 \epsilon_R(\mathbf{n}) = \left(v(R) + \frac{V_0}{a}\right)\left(1 + \mathcal{O}(\beta^{-1})\right) \quad . \tag{41}$$

The correction to this energy conserving rule reflects the fact that the local plaquette operator undergoes a renormalization. However, mean field arguments (Appendix A) suggest only small corrections. The energy sum rule is also in accord with Eq. 33.

The leading order contribution to the self energy V_0, $C_F G_L(\mathbf{0}) g^2$, merely changes sign when differentiated with respect to $\ln\beta$. As a consequence, this contribution to both the action and the energy sums diverges like $1/(a \ln a)$. Due to the localization of the self energy to the vicinity of the two sources, the peaks of the distributions diverge like $1/(a^4 \ln a)$ in physical units (or like $1/\ln a$ when measured in lattice units). The physical part $v(R)$ on the r.h.s. of the action sum rule is accompanied by an anomalous dimension $\partial \ln a / \partial \ln \beta \propto \ln a$. For this reason, the measured lattice action density σa^4 is expected to scale like $a^4 \ln a$ outside the peaks while the energy density vanishes like a^4 (in lattice units). $\mathcal{E}$ and $\mathcal{B}$ mix under renormalization group transformations since the sum of both densities carries dimension a^4 while its difference is accompanied by $a^4 \ln a$. Thus, only the energy density and the combination $(\partial \ln \beta / \partial \ln a)\sigma$ are relevant to the continuum limit.

4 Results

4.1 Static potential

To prepare the stage for the colour flux investigations, we had to calculate the static $Q\bar{Q}$ potential. It will render the string tension, which serves to fix the physical scale and relates the results, obtained at different β values to each other.

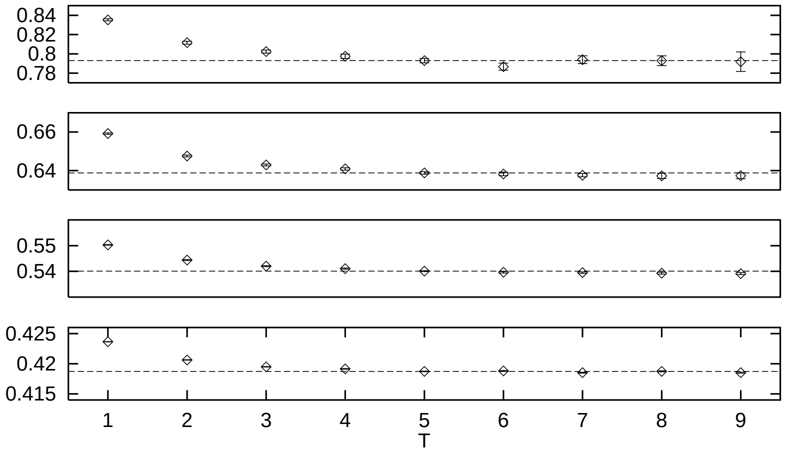

Figure 5: *$V(R,T)$ as a function of T for $R = 20$, $R = 10$, $R = 5$ and $R = 2$, respectively, at $\beta = 2.635$. The plateau values obtained at $T = 5$ are indicated by the horizontal dashed lines.*

4.1.1 Data

The potential data has been obtained by the method described in Section 2.3. Finite T approximants $V(R,T)$ and $C_0(R,T)$ to the ground state potential values and overlaps are computed according to Eqs. 14 and 15. These are traced until a plateau (in T) is reached. The numerical situation is illustrated in Fig. 5 for a few typical quark separations at $\beta = 2.635$. For the 16^4 lattice at $\beta = 2.5$ the $T_{\text{min}} = 3$ approximant has been found to agree with the plateau values while for the 32^4 lattices at $\beta = 2.5$ and $\beta = 2.74$, $T_{\text{min}} = 4$ had to be taken and at $\beta = 2.635$ we went as far as $T_{\text{min}} = 5$. To exclude any remaining systematic bias on the fitted parameters, all fits have been performed for $T = T_{\text{min}}$, and $T = T_{\text{min}} + 1$. Within statistical errors and fixed R range, the fit parameters remained stable. For larger β values, the reduced physical $t = Ta$ separations appear to be partly compensated by better ground state overlaps.

We note, that the actual value of T_{min} is not only affected by the ground state overlaps but also influenced by statistical errors that depend on the particular number of measurements, physical volume and method (link integration).

In Tabs. 2–4 we have collected results on the potential values, $V(R)$, and overlaps, $C_0(R)$, up to a physical distance of about .7 fm. This scale has been obtained from the relation $\kappa = \sqrt{K}a = 440$ MeV. For larger separations we refer to the parametrizations presented below since no systematic deviations are observed from the interpolating curve (that is dominated by the linear part of the potential). Remember, that all estimates for the potential and overlaps constitute strict upper limits to their asymptotic ($T \to \infty$) values. The paths, displayed in the second column, are numbered according

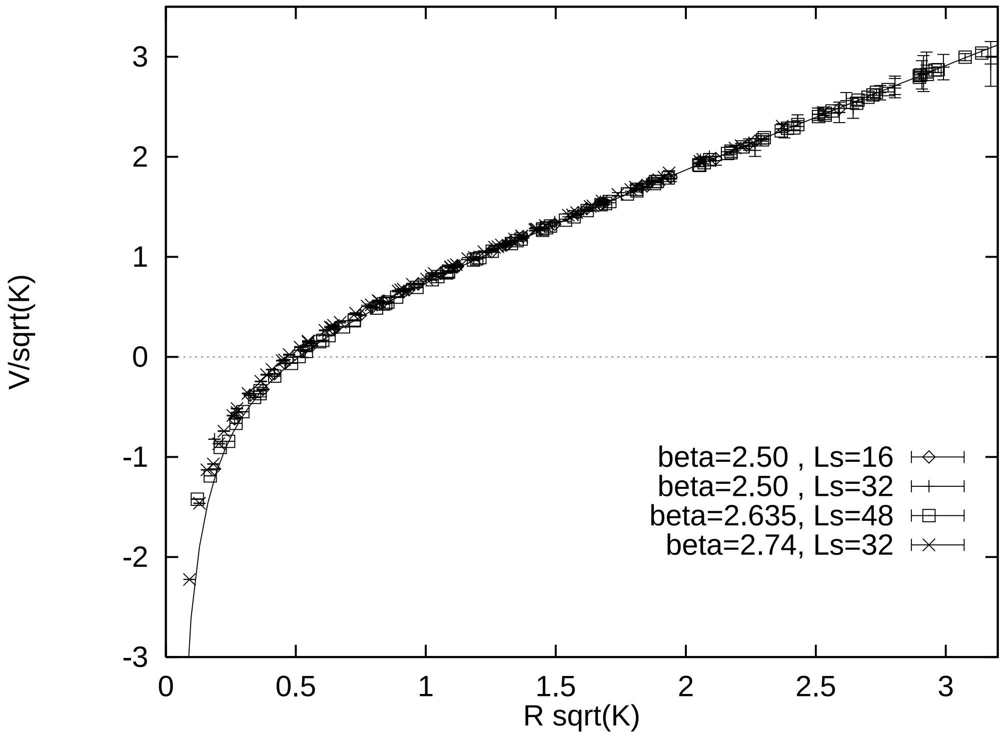

Figure 6: *The potential, measured on the four lattices, scaled in units of the string tension. The solid line refers to the string picture expectation* $V(R) = KR - \pi/(12R)$.

R	Path	$V(R)$	$C_0(R)$	R	Path	$V(R)$	$C_0(R)$
1.00	1	.3356(2)	.979(1)	4.90	5	.6671(10)	.927(3)
1.41	2	.4292(4)	.975(1)	5.00	1	.6706(9)	.930(3)
1.73	4	.4735(5)	.970(2)	5.20	4	.6817(15)	.928(5)
2.00	1	.4844(4)	.963(1)	5.66	2	.7012(14)	.921(4)
2.24	3	.5137(4)	.963(2)	6.00	1	.7137(11)	.915(3)
2.45	5	.5330(5)	.960(2)	6.00	6	.7157(13)	.916(4)
2.83	2	.5585(7)	.954(2)	6.71	3	.7418(13)	.902(4)
3.00	1	.5660(6)	.956(2)	6.93	4	.7532(23)	.904(6)
3.00	6	.5698(5)	.952(2)	7.00	1	.7537(12)	.904(4)
3.46	4	.5969(10)	.945(3)	7.07	2	.7586(17)	.904(5)
4.00	1	.6229(6)	.939(2)	7.35	5	.7701(14)	.901(4)
4.24	2	.6379(10)	.942(3)	8.00	1	.7931(16)	.890(5)
4.47	3	.6479(8)	.934(3)				

Table 2: *Potential and overlap values at* $\beta = 2.5$.

R	Path	$V(R)$	$C_0(R)$	R	Path	$V(R)$	$C_0(R)$
1.41	2	.37719(4)	.9799(1)	6.93	4	.5826(5)	.921(2)
1.73	4	.41154(7)	.9754(3)	7.00	1	.5839(4)	.923(2)
2.00	1	.41873(6)	.9694(2)	7.07	2	.5853(5)	.922(2)
2.24	3	.44040(8)	.9694(3)	7.35	5	.5909(4)	.919(2)
2.45	5	.45445(9)	.9674(4)	8.00	1	.6033(4)	.913(2)
2.83	2	.47163(12)	.9627(5)	8.49	2	.6123(7)	.908(3)
3.00	1	.47604(11)	.9620(4)	8.66	4	.6154(7)	.907(3)
3.00	6	.47937(15)	.9610(6)	8.94	3	.6202(7)	.902(3)
3.46	4	.49685(16)	.9563(7)	9.00	1	.6211(5)	.904(2)
4.00	1	.51239(14)	.9508(6)	9.00	6	.6215(7)	.902(3)
4.24	2	.52051(24)	.9512(10)	9.80	5	.6352(7)	.894(3)
4.47	3	.52678(18)	.9465(7)	9.90	2	.6367(8)	.895(4)
4.90	5	.53802(24)	.9421(10)	10.00	1	.6388(7)	.895(3)
5.00	1	.54008(20)	.9435(8)	10.39	4	.6453(10)	.888(5)
5.20	4	.54525(33)	.9403(14)	11.00	1	.6556(6)	.887(3)
5.66	2	.55598(29)	.9342(12)	11.18	3	.6580(10)	.881(4)
6.00	1	.56349(26)	.9326(13)	11.31	2	.6608(11)	.881(5)
6.00	6	.56369(34)	.9303(14)	12.00	1	.6726(10)	.880(4)
6.71	3	.57818(36)	.9248(16)	12.00	6	.6717(12)	.872(5)

Table 3: *Potential and overlap values at* $\beta = 2.635$.

to Eq. 5.

In Fig. 6 we show the familiar scaling plot for the potential in form of the combination $(V(R\sqrt{K}) - V_0)/\sqrt{K}$ with V_0 and K as obtained from the four- parameter fits, described below. Notice, that we can trace the potential up to the impressively large separation of 2.3 fm! The curve represents the string picture prediction $R - \frac{\pi}{12R}$. The nice scaling between the potentials illustrates the restoration of continuum rotational invariance at remarkably small lattice separations.

4.1.2 Potential fits

Our potential values have been fitted to the parametrizations

$$V(R) = V_0 + KR - \frac{e}{R} \tag{42}$$

and

$$V(\mathbf{R}) = V_0 + KR - \frac{e}{R} + f\left(\frac{1}{R} - \left[\frac{1}{\mathbf{R}}\right]\right) \tag{43}$$

with

$$\left[\frac{1}{\mathbf{R}}\right] = 4\pi G_L(\mathbf{R}) \quad , \tag{44}$$

R	Path	$V(R)$	$C_0(R)$	R	Path	$V(R)$	$C_0(R)$
1.00	1	.2786(1)	.959(4)	8.94	3	.5325(5)	.913(4)
1.41	2	.3480(2)	.963(4)	9.00	1	.5327(5)	.921(4)
1.73	4	.3780(2)	.953(4)	9.00	6	.5329(5)	.917(4)
2.00	1	.3837(2)	.941(4)	9.80	5	.5413(5)	.909(4)
2.24	3	.4021(2)	.945(4)	9.90	2	.5430(6)	.926(4)
2.45	5	.4137(2)	.943(4)	10.00	1	.5434(6)	.910(4)
2.83	2	.4273(3)	.933(4)	10.39	4	.5474(7)	.907(4)
3.00	1	.4308(2)	.941(4)	11.00	1	.5533(6)	.913(4)
3.00	6	.4340(3)	.937(4)	11.18	3	.5550(6)	.912(4)
3.46	4	.4483(4)	.930(4)	11.31	2	.5571(6)	.906(4)
4.00	1	.4588(3)	.927(4)	12.00	1	.5635(6)	.904(4)
4.24	2	.4654(3)	.943(4)	12.00	6	.5633(6)	.901(4)
4.47	3	.4698(3)	.926(4)	12.12	4	.5653(9)	.915(5)
4.90	5	.4780(3)	.924(4)	12.25	5	.5663(8)	.911(4)
5.00	1	.4788(3)	.932(4)	12.73	2	.5711(8)	.917(4)
5.20	4	.4831(4)	.935(4)	13.00	1	.5730(7)	.908(4)
5.66	2	.4904(4)	.922(4)	13.42	3	.5771(7)	.898(4)
6.00	1	.4950(3)	.921(4)	13.86	4	.5811(9)	.895(4)
6.00	6	.4955(4)	.919(4)	14.00	1	.5825(9)	.898(4)
6.71	3	.5055(4)	.927(4)	14.14	2	.5842(10)	.897(5)
6.93	4	.5089(5)	.919(4)	14.70	5	.5888(9)	.892(5)
7.00	1	.5085(3)	.925(4)	15.00	1	.5920(9)	.903(5)
7.07	2	.5104(4)	.933(4)	15.00	6	.5916(9)	.896(4)
7.35	5	.5135(5)	.926(5)	15.56	2	.5980(10)	.908(5)
8.00	1	.5214(5)	.916(4)	15.59	4	.5973(10)	.902(5)
8.49	2	.5273(5)	.915(4)	15.65	3	.5987(9)	.900(5)
8.66	4	.5284(7)	.923(4)	16.00	1	.6014(8)	.891(4)

Table 4: *Potential and overlap values at* $\beta = 2.74$.

where $G_L(\mathbf{R})$ is the lattice gluon propagator (Eqs. 78, 77), computed on an infinite[14] lattice. V_0, K, e, and f are the fit parameters.

In the analysis we followed the fitting procedure, described in Ref. [26]. Four different fit algorithms have been applied to the data:

- uncorrelated fits with the errors of potential values obtained on the original sample (UN),
- uncorrelated fits with errors calculated for each bootstrap separately with a subbootstrap (UB),

---

[14] The lattice sums have been computed numerically on 1024^3, 2048^3, and 4096^3 lattices and extrapolated in $1/L_S$ to their infinite volume limits.

$\beta = 2.5 \quad , \quad L_S \times L_T = 16^4$

	V_0	K	e	R_{min},R_{max}	χ^2/N_{DF}
UN	.545(3)(4)	.0348(3)(4)	.240(9)(32)	3.00,13.86	17/26
UB	.547(3)(8)	.0346(3)(7)	.244(8)(21)	3.00,13.86	19/26
CN	.547(3)(8)	.0346(3)(7)	.244(8)(20)	3.00,13.86	20/26
CB	.546(4)(14)	.0348(4)(9)	.241(9)(44)	3.00,13.86	19/26

$\beta = 2.5 \quad , \quad L_S \times L_T = 32^4$

	V_0	K	e	R_{min},R_{max}	χ^2/N_{DF}
UN	.542(3)(12)	.0354(3)(12)	.24(1)(3)	3.00,24.25	50/59
UB	.553(4)(20)	.0345(3)(14)	.27(1)(5)	4.24,24.25	34/56
CN	.553(4)(30)	.0345(4)(14)	.27(1)(7)	4.24,24.25	48/56
CB	.560(7)(20)	.0340(5)(18)	.29(2)(8)	4.00,17.32	35/44

$\beta = 2.635 \quad , \quad L_S \times L_T = 48^3 \times 64$

	V_0	K	e	R_{min},R_{max}	χ^2/N_{DF}
UN	.523(1)(6)	.01451(4)(14)	.269(2)(15)	4.00,41.57	70/95
UB	.519(1)(3)	.01466(5)(15)	.250(10)(15)	4.00,41.57	91/95
CN	.519(1)(2)	.01466(5)(14)	.251(12)(16)	4.00,41.57	92/95
CB	.518(7)(8)	.01467(25)(31)	.242(48)(62)	4.00,41.57	95/95

$\beta = 2.74 \quad , \quad L_S \times L_T = 32^4$

	V_0	K	e	R_{min},R_{max}	χ^2/N_{DF}
UN	.4816(12)(10)	.00834(6)(5)	.217(3)(5)	6.00,27.71	36/51
UB	.4816(9)(27)	.00834(4)(12)	.217(4)(14)	6.00,27.71	47/51
CN	.4816(9)(31)	.00834(4)(13)	.217(4)(17)	6.00,27.71	47/51
CB	.4817(14)(55)	.00834(6)(37)	.218(6)(89)	6.00,27.71	48/51

Table 5: *Three-parameter fits according to Eq. 42. The first column labels the fit algorithm. In the last two columns, the "best" fit range and corresponding* χ^2/N_{DF} *values are stated. The first errors are statistical only, the second errors include systematic uncertainties.*

- correlated fits with the covariance matrix computed on the original sample (CN),
- correlated fits with covariance matrices calculated on each bootstrap separately (CB).

The fit range has been adapted automatically. For each range, a quality parameter,

$$Q = \alpha \frac{N_{DF}}{N_{DF,\max}} \frac{K}{\Delta K} \quad , \tag{45}$$

of the fit has been computed from the confidence level, α. The largest quality corresponds to the "best" fit range. As a systematic error we have taken the scatter between the fit parameters from fits with $Q \geq \frac{3}{4} Q_{\max}$.

In Tabs. 5 and 6 the results are listed for three- and four- parameter fits, respectively, together with their statistical and systematic uncertainties. In addition, the "best" fit ranges and corresponding χ^2 values are included. Correlated and uncorrelated fits show

$\beta = 2.5 \quad , \quad L_S \times L_T = 16^4$

	V_0	K	e	f	R_{min}, R_{max}	χ^2/N_{DF}
UN	.545(1)(3)	.0349(2)(4)	.242(2)(5)	.244(7)(14)	1.73,13.86	19/30
UB	.545(1)(3)	.0349(2)(3)	.242(2)(5)	.248(7)(26)	1.73,13.86	19/30
CN	.545(1)(3)	.0350(2)(4)	.242(2)(5)	.248(7)(28)	1.73,13.86	20/30
CB	.545(1)(3)	.0350(3)(4)	.242(2)(5)	.245(8)(27)	1.73,13.86	20/30

$\beta = 2.5 \quad , \quad L_S \times L_T = 32^4$

	V_0	K	e	f	R_{min}, R_{max}	χ^2/N_{DF}
UN	.550(2)(6)	.0347(2)(5)	.256(5)(14)	.30(2)(9)	2.83,24.25	45/60
UB	.547(2)(10)	.0350(2)(9)	.245(4)(23)	.34(2)(14)	3.00,17.32	37/46
CN	.547(2)(9)	.0350(2)(12)	.245(5)(24)	.34(2)(15)	3.00,17.32	37/46
CB	.549(3)(14)	.0348(3)(12)	.251(9)(36)	.33(4)(14)	3.00,17.15	37/45

$\beta = 2.635 \quad , \quad L_S \times L_T = 48^3 \times 64$

	V_0	K	e	f	R_{min}, R_{max}	χ^2/N_{DF}
UN	.519(1)(2)	.01467(3)(14)	.254(2)(9)	.29(2)(11)	3.00,39.84	67/95
UB	.521(1)(2)	.01459(2)(8)	.263(2)(6)	.23(3)(9)	4.24,41.57	74/93
CN	.521(1)(2)	.01458(2)(8)	.263(1)(7)	.15(2)(8)	4.00,36.00	71/90
CB	.523(1)(3)	.01451(7)(13)	.267(4)(9)	.16(7)(15)	4.00,27.00	56/76

$\beta = 2.74 \quad , \quad L_S \times L_T = 32^4$

	V_0	K	e	f	R_{min}, R_{max}	χ^2/N_{DF}
UN	.4823(4)(7)	.00832(3)(5)	.2220(9)(21)	.21(1)(5)	2.45,26.00	38/62
UB	.4828(3)(8)	.00830(2)(4)	.2235(9)(26)	.19(1)(3)	2.83,27.71	51/62
CN	.4828(3)(5)	.00830(2)(3)	.2235(9)(15)	.19(1)(2)	2.83,27.71	51/62
CB	.4827(5)(10)	.00830(3)(6)	.2234(14)(34)	.20(2)(5)	2.83,26.00	51/61

Table 6: *Four-parameter fits according to Eq. 43. The first column labels the fit algorithm. In the last two columns, the "best" fit range and corresponding χ^2/N_{DF} values are stated. The first errors are statistical only, the second errors include systematic uncertainties.*

little difference in χ^2 values, which gives evidence that correlations between potential data at different R-values are small. In the further analysis we use the results of the CN four- parameter fits for the string tension K and self energy V_0.

As expected from perturbation theory the self energy, V_0, decreases slightly with β from $V_0 = .547$ at $\beta = 2.5$ down to $V_0 = .483$ at $\beta = 2.74$. On the two large lattice volumes, the Coulomb coefficients, e, are in agreement with the value $\pi/12 \approx .262$, as expected in the string picture. On the smaller lattice volumes they come out somewhat smaller. This might be a result of the different fit ranges: on the large lattices the fit result is dominated by the potential values from separations where the string picture is expected to be applicable. The parameter f, used to account for the lattice symmetry turns out to be of approximately the same size as e in all cases, indicating that violations of rotational symmetry can be understood in terms of the lattice one gluon exchange, contrary to $SU(3)$ where values $f \approx .6e$ have been found [7].

β	$\sqrt{K}$	$\langle\Box\rangle$	$-\tilde{B}^{-1}_{2loop}(\beta)$	$-\tilde{B}^{-1}(\beta)$
2.3	.3690(30)	.39746 (1)	5.77	7.20(13)
2.4	.2660(20)	.36352 (1)	6.04	7.28(9)
2.5	.1870(10)	.34802 (1)	6.31	7.36(8)
2.5115	.1836(13)	.34564 (1)	6.34	7.38(8)
2.635	.1208(1)	.324308(2)	6.67	7.51(6)
2.74	.0911(2)	.308721(2)	6.95	7.63(5)
2.85	.0662(6)	—	7.25	7.81(4)

Table 7: *The "β-function" $\tilde{B}^{-1}(\beta) = \partial(\ln a)/\partial(\ln\beta)$, obtained by use of the perturbative two loop approximation, and by the interpolation procedure, described in the text. The $\beta = 2.3$ and $\beta = 2.4$ values are taken from Ref. [27, 28], the $\beta = 2.5115$ value is from Ref. [29], the $\beta = 2.85$ value from Ref. [6].*

4.1.3 Determination of the β-function

From Eq. 99 it is evident that the action density diverges like

$$\tilde{B}^{-1}(\beta) = \frac{\partial \ln a}{\partial \ln \beta} = -\frac{\partial g}{\partial \ln \beta} B^{-1}(g) = \frac{g}{2} B^{-1}(g) \tag{46}$$

as a function of a (see Eq. 39), where

$$B(g) = -\frac{\partial g}{\partial \ln a} \tag{47}$$

denotes the Callan-Symanzik β-function. For this reason, we shall set out in this section to determine the β-function within the $g^2 = 2N/\beta$ region covered by our simulations.

The β-function can be expanded in terms of the coupling:

$$B(g) = -b_0 g^3 - b_1 g^5 - \cdots \tag{48}$$

with $b_0 = 11N/(48\pi^2)$ and $b_1 = 34N^2/(3(16\pi^2)^2)$. From Eqs. 47 and 48 one finds the familiar formula

$$a = \Lambda_L^{-1} f(\beta) \left(1 + \mathcal{O}(\beta^{-1})\right) \quad \text{with} \quad f(\beta) = e^{-\beta/4Nb_0} (\beta/2Nb_0)^{b_1/2b_0^2} \quad . \tag{49}$$

In Tab. 7, results for the square root of the string tension, $\sqrt{K}$, and the plaquette expectation value are collected for various β. The results are taken from the present simulation and Refs. [27, 28, 29, 6]. From Eq. 49 we obtain $f(\beta)\sqrt{K} = \sqrt{\kappa}\Lambda_L^{-1}(a)$ by using $a^2 = K/\kappa$. In Fig. 7 the a dependence of $\Lambda_{\overline{MS}}(a) = 19.82\Lambda_L(a)$ is shown. As can be seen from the non-vanishing slope, within the β region accessible by present computers, higher order contributions to the asymptotic formula Eq. 49 are important. A cut-off parameter $\Lambda_E(a)$ from the effective coupling $\beta_E = \frac{3}{4}(1-\langle\Box\rangle)^{-1}$, introduced in Ref. [30], has also been computed. This cut-off parameter is translated into the $\overline{MS}$ scheme by the relation $\Lambda_{\overline{MS}}(a) = 11.51\Lambda_E(a)$. As can be seen, the slope is substantially reduced but asymptotic scaling remains violated.

The difference between the $\Lambda^{-1}(a)$ sets indicates the size of higher order (perturbative and non-perturbative) contributions to the β-function. Within the present β range we find the points to fall quite well on straight lines (see Fig. 7)[15]; so we use a linear interpolation of our data in the region $2.4 \leq \beta \leq 2.85$, according to the parametrization

$$\Lambda_L^{-1}(a) = \Lambda_L^{-1}(0) + \eta a \quad . \tag{50}$$

From the fitted slope, η, we obtain the relation

$$a = \Lambda_L^{-1}(a=0)\frac{f(\beta)}{1-\eta f(\beta)} \tag{51}$$

and arrive at

$$\tilde{B}^{-1}(\beta) = \frac{\partial \ln f(\beta)}{\partial \ln \beta}(1-\eta f(\beta))^{-1} = \left(-\frac{\beta}{4Nb_0} + \frac{b_1}{2b_0^2}\right)(1-\eta f(\beta))^{-1} \quad . \tag{52}$$

The resulting values for $-\tilde{B}^{-1}$, obtained in the two loop approximation and by the above fit, are displayed in the fourth and fifth column of Tab. 7, respectively. Depending on how many of the points we include into our fit, we obtain values $52.2 < \eta/\sqrt{\kappa} < 59.5$. This systematic uncertainty is incorporated into the errors of the $\tilde{B}^{-1}$ values in the last column. Watch the difference between the "measured" β-function and the corresponding perturbative expression decrease with the lattice spacing, as it should be!

4.2 Colour field distributions

4.2.1 General features

We are now in the position to present a survey on the flux distributions and watch the formation of flux tubes with increasing distance between the static sources.

In Figs. 8 and 9, we display the situation at $\beta = 2.5$ and $Ra = 8a \approx .7$ fm, for the energy and action densities, respectively, in units of the string tension. Notice, that the

---

[15] However, for small a, the leading order correction should be proportional to $g^2 \propto 1/\ln a$, instead. So, it is not surprising that the linear *effective* parametrizations do not extrapolate to the same continuum limit.

mesh is not equidistant in the perpendicular direction because the off-axis separations $n_\perp \propto (1,1)$ are included. We confirm the earlier observation [3] that magnetic and electric field energies are of similar size (within 20%), i.e. definitely dominated by higher order contributions in g^2. This results in a small energy density in the middle of the flux tube, which in the case of Fig. 8 is nevertheless well above noise. The vertical axis of Fig. 8 is expanded by a factor $-\tilde{B}^{-1} = -\partial \ln a/\partial \ln \beta \approx 7.36$, relative to Fig. 9. This is suggested from the form of the sum rules (see Eqs. 39 and 41). The figures show that this is indeed a reasonable choice. The electric flux tube looks distinctly broader around the sources: contrary to the values in the physical region, the (self-interaction) values at the peaks of the action and energy density distributions roughly equal each other. This observation, which is in accord with the sum rule prediction, causes the above optical impression.

Fig. 10 illustrates the action density distribution at equal physical geometry as Fig. 9 but with finer lattice spacing ($R = 12$ on the $\beta = 2.635$ lattice). The vertical scale of Fig. 10 is contracted relative to Fig. 9 by the ratio of the corresponding two $\tilde{B}$ values. We observe nice scaling of the fields outside the peaks. The latter diverge by the expected additional factor $a_{2.5}^4/a_{2.635}^4 \approx 5$.

The elongation of the flux distribution into a tube is traced in Figs. 9, 11, and 12 for the action density. The physical source separations correspond to .7, 1, 1.35, and 1.7 fm, respectively. Our data representation avoids use of a smoothing procedure, as has been applied in previous work [31, 32]. We are in the position to judge the significance of the actual data from its intrinsic fluctuations. In this way, we are less bound to be deceived by the beauty of some graphic interpolating algorithm. Indeed, given the quality of our data, we can follow — for the first time in a lattice simulation — the flux tube along distances of up to 1.7 fm or 30 lattice sites at $\beta = 2.635$ (Fig. 12)!

4.2.2 Finite a effects

In this subsection we will start to discuss the systematic errors on our field measurements. A prominent effect would be expected from the limitation of the lattice resolution a to which we will turn first.

The comparison shown in Fig. 12 between the action density distribution at a quark separation of 1.7 fm, obtained at two different lattice spacings, indicates scaling of the results outside the self energy region. The same holds qualitatively true for the situation at a distance of .7 fm as can be seen from Figs. 9 and Fig. 10. Thus, we are driven to the conclusion that continuum results can be obtained from quark distances as small as *eight* lattice spacings, at least at positions, separated by more than two lattice sites from the sources.

Let us investigate the situation in some more detail. In Fig. 13 we compare longitudinal action flux tube profiles obtained at $\beta = 2.5$ and $\beta = 2.635$ for $r \approx .7$ fm to each other. One source is placed at the origin of the coordinate system. The data are appropriately scaled in units of the string tension and in addition divided by the expected anomalous dimensions from Tab. 7. The situation is displayed for $x_\perp \approx .17$ fm. The latter distance corresponds to $n_\perp = 2$ and $n_\perp = 3$ for the two β values, respectively. Though the data are compatible to each other within errors, the values obtained at the finer resolution tend to be systematically below the corresponding $\beta = 2.5$ values. The same is found in a comparison of transverse profiles obtained on the two data sets at the center plane between the sources (Fig. 14). However, due to the errors on the string tension values and the β-function (Notice, that the vertical axis has been scaled by a factor K^2!), a relative overall scale error between the two data sets of about 8% is expected which easily explains systematic deviations from our expectation.

We conclude that at separations $R \geq 8$ continuum action and energy density distributions can indeed be observed on the lattice. This conclusion is further supported by the fact that cylindrical rotational invariance is restored (within errors) as can be gathered from Fig. 14 where the values obtained at plane diagonal sites (multiples of $\sqrt{2}$) neatly interpolate between the values, measured along a lattice axis. As we will see in Section 5.1 violations of this rotational invariance are encountered for $R \leq 6$, even at the center plane. However, for sufficiently small lattice resolution, these violations can be understood in terms of lattice perturbation theory and eventually corrected to obtain the corresponding continuum expressions. This is beyond the scope of the present paper, where we are mainly interested in non-perturbative large distance effects.

4.2.3 Finite size effects

Lattice results for the heavy quark potential and colour flux distributions are subject to finite size effects (FSE). The impact of FSE onto (smeared) Wilson loops is twofold. The ground state potential $V(R)$ itself might depend on the finite volume, due to the infra red cut-off. Contrary to the perturbative expectation, previous lattice studies of the confined phase of $SU(2)$ and $SU(3)$ gauge theories [10, 20] show that this effect already becomes negligible for lattice extents as small as $L_S \approx 1$ fm. In the present simulation we are able to confirm this observation by comparing the 16^4 and 32^4 potential data at $\beta = 2.5$.

In addition one might worry about the impact of mirror sources, due to the toroidal structure of the lattice: if one places sources at the positions $\mathbf{0}$ and $\mathbf{R}$, the corresponding state is virtually indistinguishable from a state created by so called mirror sources. Thus, in the case of the (self adjoint) fundamental representation of $SU(2)$, one expects — in addition to a non-vanishing overlap of the creation operator with a $Q\bar{Q}$ state with separation $\mathbf{D}(\mathbf{0}) = \mathbf{R}$ — overlaps with states of internal separation $\mathbf{D}(\mathbf{n}) = \mathbf{R} + \mathbf{m}L_S$ with m_i being (not necessarily positive) integer numbers. Let us consider for the moment the "perfectly" smeared Wilson loop (with no overlap whatsoever to excited states). One would thus anticipate

$$W(\mathbf{R},T)=\sum_{\mathbf{m}} c_{\mathbf{m}} e^{-V(D(\mathbf{m}))T} \quad . \tag{53}$$

In strong coupling these mirror copy effects are exponentially suppressed as the linear size grows in all directions. For a large planar Wilson loop the leading order behaviour is:

$$W(R,T)=e^{-KRT}\left(1+e^{-K(L_SL_T-2RT)}+\cdots\right) \quad . \tag{54}$$

However, in weak coupling, perturbation theory yields $W(R,T)=W(L_S-R,L_T-T)$ in the non zero momentum sector. At least to the lowest order $(\mathcal{O}(g^2/(L_S^3L_T)))$ the zero modes do not obey this behaviour [33]. Their influence might become even more important to higher orders, especially in the infra red regime of large R.

The naïve geometrical expectation of Eq. 53 is not borne out by the data, neither for the potential nor for the action and energy densities. This can be inferred from selection rules due to symmetries of the creation operator. As we shall show in the following, this indeed happens in case of the Wilson loop, due to a symmetry under transformations by center group elements of $SU(2)$ in the fundamental representation: $Z_2=\{-1,1\}$.

Let us introduce a non-trivial center transformation to all spatial links that point into direction i and cross the hyperplane $n_i=k+1/2$:

$$\tau_k^i: U_i(n)\to -U_i(n) \quad \text{for all } n \text{ with} \quad n_i=k \quad . \tag{55}$$

Obviously, the action is invariant under this transformation since each plaquette crossing the transformation plane contains two such rotated links.

Our creation operator $\Gamma_{\mathbf{R}}^\dagger=Q(\mathbf{0})U(\mathbf{0}\to\mathbf{R})Q^\dagger(\mathbf{R})$ (Eq. 3) contains the spatial transporter $U(\mathbf{0}\to\mathbf{R})$ that is a combination of various paths connecting the two quarks. The smearing algorithm (Eq. 13) only permits continuous deformations of the straight path. Thus, all paths cross the hyper planes $n_i=0,\ldots,R_i-1$ an odd number of times while all other planes are crossed an even number of times. Therefore, $\Gamma_{\mathbf{R}}^\dagger|0\rangle$ is an eigenstate of τ_k^i:

$$\tau_k^i\Gamma_{\mathbf{R}}^\dagger=\left\{\begin{array}{ccl} -\Gamma_{\mathbf{R}}^\dagger & , & 0\le k<R_i \\ \Gamma_{\mathbf{R}}^\dagger & , & \text{elsewhere}\end{array}\right. \quad . \tag{56}$$

As the eigenvalues remain invariant under the Hamiltonian evolution they serve as conserved quantum numbers. Consequently, in case of the gauge group $SU(2)$, only coefficients $c_{\mathbf{m}}$ with *even* m_i are different from *zero* in Eq. 53. Therefore, the effective "periodicity"[16] is $2L_S$ rather than L_S. For example, the leading order "pollution" for the on-axis separation R carries the decay constant $V(2L_S-R)$. For a linearly rising

---

[16] Obviously, the coefficients $c_{\mathbf{m}}$ can differ from each other, depending on the path combination, appearing in the transporter $U(\mathbf{0}\to\mathbf{R})$, unless $R_i=mL_S$.

long range potential, these large exponents cause a strong suppression of fake states. This explains why such effects remain unseen in the present simulation, even at R as large as $3/4L_S$.

The above arguments can be generalized to the local field strength measurement operators $O_R(\mathbf{n}) = \epsilon_R(\mathbf{n}), \sigma_R(\mathbf{n})$. O_R has no overlap to a $Q\bar{Q}$ state, separated by $L_S - R$. The only relevant finite size effects stem from the periodicity

$$O_R(\mathbf{n}) = O_R(L_S - n_1, L_S - n_2, L_S - n_3) \quad . \tag{57}$$

For $\mathbf{n}$ taken along the $Q\bar{Q}$ axis, energy and action densities are strongly suppressed outside the sources: in case of a dipole field (the leading order perturbative expectation, Eq. 32) the action and energy densities fall off like $(|n_1| - R/2)^{-4}$ for $|n_1| > R/2$. Thus, FSE into the longitudinal direction are negligible. The $n_\perp$ distributions are more sensitive to FSE as will be explained in Appendix D (see also Fig. 3).

A comparison of the potential computed on 16^4 and 32^4 lattices at $\beta = 2.5$ shows no statistically significant bias due to the volume[17]. The same holds true for the action and energy density distributions as a comparison between the two lattice volumes shows for the largest $Q\bar{Q}$ separation realized on the smaller lattice, $R = 8$ (where FSE should be strongest). As an example, the two data sets are displayed in Fig. 15 for the longitudinal slice $n_\perp = 2$. Fig. 16 shows the corresponding transverse distributions for $n_1 = 0$.

Since the $\beta = 2.635$ lattice is comparable in physical size to the 32^4 lattice at $\beta = 2.5$ while the $\beta = 2.74$ lattice has about the same physical extent as the 16^4 lattice, we conclude that all our lattices are sufficiently large for the present purpose and that FSE are below the statistical accuracy of the present investigation.

4.2.4 T-stability

In the two preceding subsections limitations in the lattice geometry have been discussed to substantiate the relevance of our lattice results to continuum physics. Here, we address the reliability of our ground state results in view of the (necessarily) limited temporal extent of the lattice operators. We will explain in some detail how the $(T \to \infty)$ results shown above have been obtained.

For the potential from unsmeared Wilson loops, one has to take $T \gg R$ in order to obtain asymptotic results as a consequence of Eq. 18. In the case of field strength

---

[17] The ground state overlaps tend to be smaller on the larger lattice, though the same smearing procedure has been applied. We suspect that the number of smearing steps needs to be increased when working on larger lattices due to a more extended wave function. However, within our statistical accuracy, this is not in the colour field distributions.

operators this amounts to $T \gg 2R$ since excitations are damped by a decay constant $\Delta V(R)/2$ only (instead of $\Delta V(R)$). For large R values, in which we are interested, it is practically impossible to obtain signals at sufficiently large T. However, this situation is considerably improved by the smearing procedure, described in Section 2.3. This is evident from Fig. 17 that presents a comparison between smeared and unsmeared results for the energy density in the center between two sources, separated by $R = 4$ at $\beta = 2.74$. Notice the logarithmic scale!

To all our (smeared) data we have performed four parameter fits according to Eq. 25 as well as two- and three-parameter fits of the form

$$\begin{aligned} \langle \Box(S)\rangle_W &= \langle\Box\rangle_{|0,R\rangle-|0\rangle} \\ &+ c_1 e^{-\pi T/R}\cosh(2\pi S/R) \\ &+ c_2 e^{-2\pi(T-2S)/R} \quad , \end{aligned} \tag{58}$$

where $\langle\Box\rangle_{|0,R\rangle-|0\rangle}$ and c_i are the fit parameters. In case of two parameter fits, c_2 is constrained to *zero*. We note that, because of the different temporal positions of magnetic and electric insertions (i.e. different values of S at fixed T), the fits have been performed separately before combining the expectation values for $\mathcal{E}$ and $\mathcal{B}$ to the energy and action densities, ϵ and σ.

In all cases, the agreement with our data was remarkable with χ^2/N_{DF} values close to *one*. For the two parameter fits we had to exclude the $T = 1$ data point. The best results have been obtained with the three-parameter fits. In case of four parameters, c_3 was found to agree with *zero* within the (large) statistical uncertainty. Within errors, the $T \to \infty$ extrapolated values coincided with the $T = 3$ value for large R and the $T = 4$ value for small R in all cases. All our results refer to the extrapolated values whose errors have been obtained by the bootstrap method [34].

In Figs. 18 and 19 we exemplify the time dependence of the electric and magnetic energy density estimates, $\mathcal{E}$ and $\mathcal{B}$, at $\beta = 2.5$ for a quark separation $R = 6$ at the position $n_1 = 0$, $n_\perp = 3$. The corresponding two-, three-, and four-parameter fits are included, together with the $T \to \infty$ extrapolated values. Due to the early ground state dominance, the fits yield fairly stable results. Notice, that due to the fact that the distance S of the plaquette insertions from the central time slice alternates with T, the parametrizations are discontinuous. For this reason, the fit values are just indicated at integer values of T. In case of integrated quantities, needed for computation of the width of the flux tube and comparison with the energy and action sum rules, the summation was first performed over the electric and magnetic energy densities for fixed T, separately, and the T-extrapolation was carried out subsequently, before combining the components to the energy and action densities.

5 Physics analysis

Having presented and substantiated our numerical results we are now ready to enter the physics analysis.

5.1 Transverse shape

We will focus on the transverse profile of field distributions in the center plane of the flux tube. For small separation of the sources, r, perturbation theory is likely to apply, and one might thus expect the (energy and action) distributions to follow the shape of the dipole field (see Eq. 32)

$$f_d(n_\perp) = \frac{1}{(4\pi)} \frac{4\delta^2}{\left(\delta^2 + n_\perp^2\right)^3} \quad , \tag{59}$$

where the width of the flux tube would increase linearly with R: $\delta = R/2$. In lowest order this would be multiplied by $C_F\alpha$ with $\alpha = g^2/(4\pi)$.

For small R, the continuum form of Eq. 59 needs be replaced by a lattice sum, $f_l(n_\perp)$, that can be computed from Eqs. 83 and 84. Remember, that this is only the leading order perturbative expectation. The data reveals that restoration of rotational invariance takes place at unexpectedly small separations, especially in the action density. To account for these higher order effects, that cancel lattice artefacts in a subtle way, we will also allow for a mixture of both, lattice and continuum expressions.

As the source separation becomes large, compared to the transverse size of the object, the string picture comes into play and we might expect (at least for small $n_\perp$) the flux distributions to be proportional to

$$f_g(n_\perp) = \frac{1}{2\pi\delta^4} \exp\left(-\frac{n_\perp^2}{\delta^2}\right) \quad . \tag{60}$$

The normalization has been chosen such that

$$\sum_{n_\perp} f_l(n_\perp) \approx \int d^2 n_\perp f_c(n_\perp) = \int d^2 n_\perp f_g(n_\perp) = \frac{1}{2\delta^2} \tag{61}$$

to allow for a direct comparison of the fitted coefficients. The question arises how the lattice data might connect between the two regimes. We will attempt to model the transition region by fits to the dipole parametrization, $f_c(n_\perp)$, with δ treated as free parameter. This is motivated by the idea that due to antiscreening of the colour sources, their effective charge increases when viewed at increasing distance from the $Q\bar{Q}$ axis, $n_\perp$, which is tantamount to a rescaling of R.

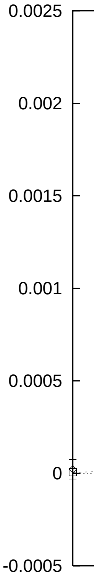

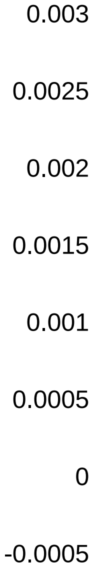

R	method	c_1	c_2	δ	A	χ^2/N_{DF}
2	1	—	0.043 (1)	1	0.0223(2)	16.0
2	2	0.0711(8)	—	1	0.0356(4)	17.4
2	3	0.0296(8)	0.0252(5)	1	0.0280(5)	15.6
2	4	0.0570(10)	—	0.90(1)	0.0354(8)	1.6
2	6	0.0310(3)	—	0.65(1)	0.0368(5)	7.4
4	1	—	0.082(2)	2	0.0142(3)	1.2
4	2	0.162(3)	—	2	0.0205(4)	5.5
4	3	0.017(3)	0.074(2)	2	0.0150(6)	1.2
4	4	0.065(7)	—	1.55(5)	0.0136(17)	0.9
4	5	0.001(2)	0.077(8)	1.09(1)	0.0134(14)	1.3
4	6	0.023(2)	—	1.01(3)	0.011 (1)	1.6
4	7	0.011(4)	0.040(10)	1.03(6)	0.012 (3)	0.8
6	1	—	0.110(6)	3	0.0086(4)	1.9
6	2	0.166(9)	—	3	0.0095(5)	1.5
6	6	0.090(30)	—	2.2 (2)	0.0090(30)	1.6
8	1	—	0.210(20)	4	0.0082(8)	0.8
8	2	0.260(30)	—	4	0.0087(10)	0.8

Table 8: *Results of fits to the central transverse profile of the energy density distribution at* $\beta = 2.5$. c_1*,* c_2*, and* δ *are fit parameters.* A *is the integrated area.*

R	method	c_1	c_2	δ	A	χ^2/N_{DF}
2	1	—	0.0271(5)	1	0.0143(3)	3.7
2	2	0.0446(8)	—	1	0.0223(4)	1.3
2	3	0.0383(8)	0.0039(5)	1	0.0211(5)	1.3
2	6	0.0230(9)	—	0.83(3)	0.0160(10)	1.6
4	1	—	0.052(1)	2	0.0093(2)	1.0
4	2	0.102(2)	—	2	0.0128(3)	3.3
4	3	0.019(2)	0.043(1)	2	0.0101(4)	0.9
4	4	0.045(5)	—	1.59(5)	0.009 (1)	0.5
4	5	0.040(10)	0.010(10)	1.59(6)	0.010 (3)	0.5
4	6	0.016(2)	—	1.03(3)	0.008 (1)	0.9
4	7	0.009(3)	0.025(8)	1.06(5)	0.007 (2)	0.5
6	1	—	0.063(4)	3	0.0054(4)	0.5
6	2	0.096(6)	—	3	0.0054(4)	0.4
6	3	0.090(6)	0.004(4)	3	0.0053(4)	0.4
6	5	0.000(1)	0.068(4)	0.3(8)	0.0058(4)	0.5
8	1	—	0.13(1)	4	0.0063(5)	1.1
8	2	0.170(20)	—	4	0.0055(6)	1.3
8	5	0.000(1)	0.13(2)	1 (3)	0.0063(10)	1.2
8	7	0.000(1)	0.13(2)	0.9(9)	0.0063(10)	1.2

Table 9: *Same as Tab. 8 for the energy density profile at* $\beta = 2.635$.

R	method	c_1	c_2	δ	A	χ^2/N_{DF}
2	1	—	0.1395(6)	1	0.0734(3)	437.7
2	2	0.234(1)	—	1	0.1171(5)	443.6
2	3	0.105(1)	0.0774(6)	1	0.093 (1)	455.0
2	4	0.468(6)	—	1.381(8)	0.123 (2)	41.6
2	5	0.560(10)	0.052 (2)	1.77 (2)	0.114(3)	3.9
2	6	0.217(3)	—	1.034(7)	0.101(2)	156.0
2	7	0.247(6)	0.064 (1)	1.35 (1)	0.101(2)	12.1
4	1	—	0.304(2)	2	0.0527(4)	174.4
4	2	0.62(1)	—	2	0.0783(5)	65.5
4	4	1.81(7)	—	2.69(3)	0.128 (6)	11.8
4	6	0.64(2)	—	1.75(2)	0.103 (5)	32.7
4	7	1.15(7)	0.131(5)	2.37(5)	0.125 (9)	5.4
6	1	—	1.11(2)	3	0.087(2)	19.0
6	2	1.67(3)	—	3	0.096(2)	14.7
6	3	1.65(3)	0.01(2)	3	0.096(2)	15.7
6	4	5.7 (5)	—	4.2 (1)	0.17 (2)	1.9
6	6	2.2 (2)	—	2.82(6)	0.13 (1)	3.7
8	1	—	2.40(3)	4	0.093(1)	12.7
8	2	3.03(4)	—	4	0.101(1)	20.0
8	4	10.1 (7)	—	5.6 (1)	0.184(14)	1.2
8	6	3.7 (2)	—	3.72(7)	0.13 (1)	2.9
10	4	14 (1)	—	6.3(2)	0.21(2)	1.5
10	6	5.1(4)	—	4.2(1)	0.15(1)	2.5
12	4	18 (1)	—	6.8(4)	0.23(3)	1.0
12	6	6.5(7)	—	4.5(1)	0.16(2)	1.2
14	4	27(1)	—	7.8(2)	0.27(2)	1.4
14	6	10(1)	—	5.2(2)	0.18(3)	1.0
16	4	19(1)	—	7.4(2)	0.21(2)	1.0
16	6	7(1)	—	4.9(3)	0.15(3)	0.8
18	4	38(2)	—	9.4(2)	0.26(2)	1.1
18	6	13(7)	—	6.1(3)	0.17(1)	1.0
20	4	16(1)	—	7.2(2)	0.19(2)	0.6
20	6	6(1)	—	4.7(3)	0.13(2)	0.6
22	6	12(1)	—	5.8(2)	0.18(1)	1.4
24	6	13(2)	—	6.1(3)	0.18(2)	0.7

Table 10: *Same as Tab. 8 for the action density profile at* $\beta = 2.5$.

In this heuristic spirit, a wide variety of one-, two- and three-parameter fits (with free parameters c_1, c_2, and δ) have been performed on the data, which are listed here in shorthand notation:

1. $c_2 f_l(n_\perp)$,
2. $c_1 f_d(n_\perp)$ with $\delta = R/2$,
3. $c_1 f_d(n_\perp) + c_2 f_l(n_\perp)$ with $\delta = R/2$,
4. $c_1 f_d(n_\perp;\delta)$,
5. $c_1 f_d(n_\perp;\delta) + c_2 f_l(n_\perp)$,
6. $c_1 f_g(n_\perp;\delta)$, and
7. $c_1 f_g(n_\perp;\delta) + c_2 f_l(n_\perp)$.

The stable fit results are collected in Tabs. 8–**??** which also contain the integrated area,

$$A = \frac{c_1}{2\delta^2} \quad \left(+\frac{2c_2}{R^2}\right) \quad . \tag{62}$$

The formula is only exact in the infinite volume limit. The second term has been corrected by numerical computations of the corresponding lattice sums. In case of the Gaussian and dipole parametrizations, additional fits, according to the finite volume expressions, derived in Appendix D (Eq. 118), have been performed. Subsequently, the results have been corrected for the finite volume in the way, described in the appendix. For the Gaussian profile the finite size corrections on the integrated area are negligible (below .2%). However, in case of a dipole distribution, though δ is little affected by FSE (up to 4%), the impact on the area is substantial (up to 25% at large R !).

In case of the dipole fits to the energy density, the combination $c_1 + c_2 = C_F\alpha_c(R)$ amounts to a kind of effective coupling on the scale R. Notice, that the odd numbered ansätze incorporate the lattice expression, f_l, while the forms (2), (4), and (6) only involve continuum formulae. Ansätze (1) and (2) require one parameter only, while (3), (4), (6) are based on two and (5), (7) on three parameters.

Energy profile We start with the discussion of the energy density data. We will concentrate the analysis mainly on the preformation of flux tubes, along the guidelines of perturbative prejudice. For our energy density resolution is not yet high enough to map out the proper string region, $r > .75$ fm.

At $\beta = 2.5$ and $R = 2$ the data is very precise and excludes the one-parameter fits (1) and (2) as well as the two parameter fit with constrained width (3). The first acceptable results are reached with ansatz (4), yielding a width[18] $\delta \approx .9$ The situation is visualized in Fig. 20 where we compare ansätze (1) and (4) against the data[19].

This situation changes at $R = 4$ where ansatz (1) leads to good results at both β values (while (2) fails), as can be seen from Figs. 21 and 22. Ansätze (3) and (5) yield results of equal quality with $c_1 \ll c_2$ which fits very nicely into the lattice perturbative picture. The data can also be parametrized by a continuum dipole with width $\delta \approx 1.55$ (ansatz (4)). However, the result of ansatz (5) ($c_1 \ll c_2$) shows that the data prefers the (one-parameter) lattice expression to the (two-parameter) continuum expression. At $R = 6$ statistical errors allow for all parametrizations (apart from occasional numerical instabilities).

We conclude that qualitatively the $R = 2$ data is described by leading order lattice perturbation theory while the $R = 4$ and $R = 6$ data can be quantitatively understood along this line.

It is gratifying to see that the effective coupling parameter $\alpha_c(R)$ increases with R, as is expected from asymptotic freedom. For $\beta = 2.5$ we obtain values ranging from $.06 < \alpha_c^2(2a) < .075$ (under exclusion of $n_\perp = 0$) over $.105 < \alpha_c^2(4a) < .125$ up to $.145 < \alpha_c^2(6a) < .225$ while at $\beta = 2.635$ we find the ranges $.055 < \alpha_c^2(2a) < .060$, $.065 < \alpha_c^2(4a) < .085$ and $.085 < \alpha_c^2(6a) < .13$, respectively. We note, that $4a_{2.5} \approx 6a_{2.635}$. Thus, these numbers give a consistent picture and should be put in perspective to the bare couplings $\alpha = 2N/(4\pi\beta) \approx .127$ and $\alpha \approx .121$ for $\beta = 2.5$ and $\beta = 2.635$, respectively.

Action profile In case of the action density, a pure lattice Coulomb ansatz is expected to fail since the action density is largely due to higher order effects. Nonetheless, it would be interesting to see whether an admixture of this term within the parametrization remains necessary to account for lattice artefacts.

It turns out that this heuristic approach looks little promising as all fits to the $R = 2$ and $R = 4$ action data yield values $\chi^2 \gg N_{DF}$[20]. Among the fits, the three-parameter forms (5) and (7) come closest to being successful. The fits are not good enough, however, to decide whether this gives genuine evidence for perturbative lattice effects or trivially reflects the higher flexibility of a three-parameter ansatz.

From $R = 6$ up to $R = 10$ ($R = 8$ at $\beta = 2.635$) the dipole fits with unconstrained

---

[18] The deviation from the expected value, $\delta = 1$, can be attributed to the fact that for small R the lattice dipole tends to be more narrow than its continuum counter part (Fig. 4).

[19] Excluding the point $n_\perp = 0$, we also find acceptable fits with methods (2) and (3). The same is the case at $\beta = 2.635$ where, due to the link integration procedure, no data point is available at this position. It is interesting to see from the large coefficient c_1, that the data prefers the continuum dipole over the lattice dipole.

[20] The $\beta = 2.635$, $R = 2$ data is exceptional since in this case we have omitted the $n_\perp = 0$ point from our fits.

width (4) appear to be the best parametrization of the data. Beyond these R-values, we observe the data being equally well described by ansatz (4) and (6) at $\beta = 2.5$, while at $\beta = 2.635$ from $R = 10$ onwards the Gaussian parametrization turns out to be more robust than the dipole ansatz against statistical fluctuations. From $R = 12$ onwards the other fitting methods also started yielding $\chi^2 \approx N_{DF}$ values. Since these fits are unphysical in this region we have not included them into the table.

The quality of the dipole (4) and Gauss (6) fits is exhibited for source separations $R = 8$ and $R = 12$ at $\beta = 2.5$ in Figs. **??** and 24, respectively.

In conclusion, leading order lattice perturbation theory is found to describe the energy density data well at small R. The fitted amplitude is in accord with asymptotic freedom. The lattice dipole term helps finding a parametrization for action density data at small R, though it is not a dominant term. Continuum dipole fits to the action yield acceptable results from distances of about 0.5 fm onwards. Up to 1 fm this continuum parametrization has a width larger than $R/2$. This effect is at variance with the antiscreening picture of colour sources and might well be a lattice artefact since a lattice dipole is broader than a continuum dipole in this R region (see Fig. 3). For larger R, the combination $2\delta/R$ decreases to values substantially below 1. From a separation of 1 fm onwards the Gaussian parametrization yields an equally good (and occasionally superior) description of the data.

5.2 String formation

When the sources are adiabatically pulled apart, the accretion of action density, $\Delta\sigma$, should — according to the string picture — be strictly localized in the center plane between the sources. This holds for R large enough compared to the other inherent length scales in the problem, i.e. the transverse width of the tube and the size of the Coulomb dominated region. It is not *a priori* obvious when this R-asymptotia sets in. The accretion phenomenon will be exploited to determine this transition point to genuine string formation.

For this purpose, we differentiate the action density distributions with respect to an increase in the source separation. This is done by computing the change, $\Delta\sigma_R = \sigma_R - \sigma_{R-2}$, under stretches $(R-2) \to R$.

In Fig. 25 we display the results for $\beta = 2.5$ and $R = 6$, 8, and 10, respectively. At $r = 10a \approx .85$ fm, we find impressive evidence that $\Delta\sigma$ is in fact zero outside the center plane! This does not hold at smaller separations, where $\Delta\sigma$ exhibits a net flow of action into the center plane from the next neighbour planes. This latter feature is in accord with the dipole picture described in Section 3.1. This action flow is a substantial effect at $R = 6$ and decreases to the 5% level at $R = 8$. Within our resolution we thus conclude, that the transition point to string formation is located at[21] $R \approx 9$.

We might view the above analysis as a differential diagnosis of flux tube formation, which provides much more sensitivity than the more conventional global tool offered by the potential. In fact, the $R = 9$ transition point into the string regime appears to be rather deep in the asymptotia of the linear part of the confining potential: it corresponds to the point $R\sqrt{K} = 1.7$ in Fig. 6, which in physical units is .75 fm!

5.3 Sum rules

Within the string regime, $Ra > .75$ fm, one can write a differential version of the sum rules:

$$\begin{aligned} F(\sqrt{R^2-1}) &= \frac{1}{2}\left(V(R-1) - V(R+1)\right) && (63)\\ &= -\frac{a^3}{2}\sum_{n_2,n_3}\left(\epsilon_{R-1}(0,n_2,n_3) + \epsilon_{R+1}(0,n_2,n_3)\right) + \mathcal{O}(\beta^{-1}) && (64)\\ &\approx -a\pi\int_0^{x_{cut}} dx\, x\left(\epsilon_{R-1}(0,x) + \epsilon_{R+1}(0,x)\right) \quad . && (65)\end{aligned}$$

For the second equality we have assumed rotational invariance and large x_{cut}. Likewise we can write a differential action sum rule[22]:

$$F(\sqrt{R^2-1}) \approx a\pi\tilde{B}(\beta)\int_0^{x_{cut}} dx\, x\left(\sigma_{R-1}(0,x) + \sigma_{R+1}(0,x)\right) \quad . \qquad (66)$$

Notice, that the fundamental assumption made for the differential version of the sum rules is only justified for $R + 1 \geq 9$ at $\beta = 2.5$. Also, the data has to exhibit approximate rotational invariance and x_{cut} has to be chosen sufficiently large. We start from numerically integrating the data. In varying x_{cut} we try to find a plateau. For $R+1 \leq 10$ a clear plateau is established while for the $R+1 > 10$ data, $x_{cut} = 10a$, the maximal distance for which we have performed measurements, had to be chosen. Thus, these values are only lower limits on the r.h.s. of Eqs. 65 and 66.

As can be seen from Fig. 26 the action sum rule is consistent with our data for $R+1 \geq 6$. This lends further support to the asymptotic character of our data (in T). Violations of rotational invariance appear to be small beyond the two directions on which we have performed our measurements. Consistency of the energy density data with the sum rule is found, albeit within reduced statistical accuracy.

---

[21] Strictly speaking, there is of course no transition point into the asymptotic regime, since the transition is smooth!

[22] The anomalous dimension of the action density outside the sources and adjacent sites equals $\tilde{B}(\beta)$, independent of the position, $\mathbf{n}$.

The fitted integrated action density, A (rescaled by the factor $\tilde{B}$), obtained in Section 5.1 (Tab. 10), is also shown in Fig. 26 for a Gaussian and a dipole transverse shape of the flux tube. The Gauss values are substantially smaller than suggested by the force. This discrepancy can only be due to a slower $n_\perp \to \infty$ fall-off of the data than assumed by the Gauss ansatz. Notice, that the string picture is only applicable for small transverse fluctuations while a large portion of the integral stems from the area of large $n_\perp$. The dipole values are consistent with the force for large separations R. It remains to be clarified whether this is just a lucky coincidence. At least for .75 fm$< r <$ 1.5 fm the large $n_\perp$ data also seems to be underestimated by a dipole shape. The functional form of the profile can be studied in more detail by varying the transverse spatial volume and exploiting the observed FSE (Appendix D).

5.4 Width of the flux tube

In addition to the (parametrization dependent) results on the width of the flux tube of Section 5.1 (Tabs. 8–**??**), we attempt to compute this important parameter by direct numerical integration:

$$\delta_\sigma^2 = \frac{\int_0^{n_{cut}} dn_\perp\, n_\perp^3 \sigma(0,n_\perp)}{\int_0^{n_{cut}} dn_\perp\, n_\perp \sigma(0,n_\perp)} \quad . \tag{67}$$

The results, including their systematic errors from varying n_{cut}, are displayed in Fig. 27, together with the expectations from the above dipole and Gauss fits. We realize that this method is not a viable way to determine the R dependence of δ: the relative error, $\Delta\delta$, of the numerical integration is intolerably large and the two fit results also differ by a factor of about 1.5. This, of course, is related to the large weight with which large $n_\perp$ points contribute to Eq. 67. For $R \geq 10$ the data is well described, both by a dipole and by a Gaussian parametrization for our $n_\perp$ window within statistical errors, and yet the two parametrizations differ substantially at large $n_\perp$.

The data on the numerically integrated widths for physical distances below .5 fm (the largest separation at which numerical integration of the energy density data could be performed) exhibits that the energy density values fall onto the line $\delta = R/2$ while the action density values are significantly larger. This tendency has also been observed in Ref. [3] and is consistent with our fit results (Tabs. 8 and 10).

An alternative approach to study the functional dependence, $\delta(R)$, is to constrain the center plane analysis to the results of the differential action sum rule. In addition, we apply a geometric method that will correlate results from different R-values to the extent that we end up with reduced relative errors and all uncertainty cast into a large overall scale error. To quote the assumptions:

1. Accretion of additional energy and action when pulling the sources apart is localized in the center plane.

2. At sufficiently large R, the change of the transverse shape under variations of R can be absorbed into two (independent) scale transformations.

Assumption (1) has been verified from our data in Section 5.2 for distances $r > .75$ fm and $\beta \geq 2.5$. Within our statistical errors, assumption (2) is also fulfilled in this region, according to the fit results in Tabs. 10 and **??**.

In this case, we can define:

$$\delta^2 = \gamma \frac{A}{\pi h} \quad . \tag{68}$$

A is the area below the curve. It can be fixed by the sum rules with high accuracy. For the action density we obtain A from

$$A = \tilde{B}^{-1}(\beta)(V(R) - V(R-1)) \quad . \tag{69}$$

Note, that here we have taken an asymmetric derivative of the potential. In case of the energy density, A directly equals the force, up to a renormalization constant. h denotes the action/energy density in the middle of the tube ($\mathbf{n} = \mathbf{0}$). γ is a geometry factor. Depending on the parametrization it can take the following values[23]:

- $\gamma = \frac{1}{2}$ for a distribution, constant for $n_\perp < n_{\max}$ and *zero* outside of this circle,
- $\gamma = 1$ for a Gaussian shape,
- $\gamma = 2$ for a dipole shape and
- $\gamma = 3$ for an $\exp(-c|n_\perp|)$ shape.

By employing the definition Eq. 68, a large portion of the error on the width is cast into the (overall) uncertainty of the geometry factor γ.

In addition to data, obtained by use of the other methods, we have included the data from this geometric method into Fig. 27 for the case $\gamma = 1$ (triangles). The differences between these points and the Gauss fits (crosses) reflect the fact that the large $n_\perp$ data is not well approximated by the Gaussian form. Remember, that this very effect has also led to an underestimation of the force in Fig. 26.

In Fig. **??**, we display our geometric results ($\gamma = 1$) for the action and energy densities at $\beta = 2.5$ and $\beta = 2.635$, scaled in units of the string tension. The dashed vertical line denotes the distance .75 fm above which the geometrical approximation is justified. As can be seen, the data exhibits scaling even below this limit. The width of the energy density starts out to be smaller than the width of the action density, as has been observed in Ref. [3], but increases faster. It then reaches the same magnitude as the action density width, before it disappears under the noise level at about .8 fm.

Above $r = 1$ fm the action density data is in agreement with a constant value

$$\delta_\sigma a \approx 1.17\sqrt{\gamma/\kappa} \approx 0.52\,\mathrm{fm}\sqrt{\gamma} \quad , \tag{70}$$

where we expect γ to take values between *one* and *two*. Logarithmic fits to the $r > 1$ fm data according to the string picture expectation, Eq. 37, yield values

$$R_0\sqrt{K} < 1/3 \quad . \tag{71}$$

No lower limit is imposed on the cut-off since the data is also in agreement with a constant. A curve with parametrization $R_0\sqrt{K} = 1/3$ and $\delta_0\sqrt{K/\gamma} = 0.5$ is indicated in Fig. **??**.

The strong parametrization dependence of the r.m.s. width, δ, is reflected in the difference by a factor of about 1.5 between the Gaussian and the dipole parametrizations (and by the different geometry factors, γ). The half width, ρ, is much less sensitive to the parametrization: both forms are valid interpolations of the data in the small $n_\perp$ region. For the two parametrizations, ρ can be connected to δ by the following relations:

$$\rho = 2\delta\sqrt{\ln 2} \approx 1.67\,\delta \qquad \text{(Gauss)} \quad , \tag{72}$$

$$\rho = 2\delta\sqrt{2^{1/3} - 1} \approx 1.02\,\delta \quad \text{(dipole)} \quad . \tag{73}$$

The resulting half widths for energy and action densities in units of the string tension are displayed in Fig. 29. We have attempted a finite volume correction to the dipole results by fitting the data to the functional form, described in Appendix D (Eq. 118), and subsequently converting the resulting δ_∞ values into ρ via Eq. 73. This amounts to a reduction of δ by less than 10%. Differences between the uncorrected dipole data and the Gauss results (up to 6%) reflect the systematic uncertainty due to the form of the interpolating curve. We observe nice scaling between both β values. We also confirm the width of the energy flux tube to be smaller than the width of the action flux tube for distances below .5 fm. Both densities increase till $r \approx 1.1$ fm. The action density saturates at the level $\rho \approx .7$ fm.

We conclude that the data beyond 1 fm is in agreement with a constant but does not contradict the expected string picture behaviour either. However, the ultra violet cut-off, r_0^{-1}, of the effective string theory is found to be larger than $3\sqrt{\sigma}$ or 1.3 GeV. This has to be compared with a lattice resolution of 2.35 or 3.64 GeV at $\beta = 2.5$ and $\beta = 2.635$, respectively. Thus, we are not too far away from the limit of applicability of the string theory.

---

[23] Note, that these values only apply to the infinite volume case. At large δ/L_S, they tend to be smaller.

6 Summary and conclusions

We have demonstrated that Wilson loop plaquette correlations offer a viable access to a lattice study of the flux tube problem on the required length scale of one to two fm.

Prior to a workable application of this tool one must ascertain an essential improvement of the lattice observation technique: the crucial ingredient of our method is the smearing of the parallel transporter within the bilocal $Q\bar{Q}$ creation operator. This secures a controlled ground state preparation of long flux tubes within few lattice time slices. Smearing is combined with integration on the time-like links of the Wilson loop to cut noise.

As a result, we can observe flux formation in the action density over lengths well beyond 1.5 fm with spatial resolution .05 fm. We find that — due to a center group symmetry of the Wilson loop — finite size effects remain well below the level of accuracy reached in the present simulation, at least as long as L_S is kept larger than 1.3 fm and $R \leq \frac{3}{4}L_S$. In particular, there are manifestly no effects of L_S-periodic distortions of the field distribution or potential due to mirror sources[24]. This implies that we can safely accommodate a flux tube of length 1.9 fm on our largest lattice of volume $(2.7 \text{ fm})^4$! The energy and action densities exhibit the expected scaling behaviour, and are consistent with the potential measurements through Michael's sum rules.

At small distances the flux tube is corrupted by lattice artefacts, which can be understood in terms of lattice perturbation theory. This holds in particular for the self energy peak around the sources, whose non-scaling behaviour is well in accord with perturbative expectations.

The transverse r.m.s. width of the action flux distribution in the midplane between the sources rises with source separation, r, until it reaches a rather constant level for separations between 1 and 2 fm. The physical value for this constant remains model dependent and ranges between .5 and .75 fm, as we estimated from a set of transverse profiles, supplementing our measurements with various plausible assumptions on the large $n_\perp$ behaviour. For the half width we find a plateau value of $\rho \approx .7$ fm. In the preasymptotic domain, the action width is observed to rise by a factor six, distinctly majoring the width of the energy distribution, before both reach their (common ?) plateau values. A logarithmic increase as suggested by string pictures for the "asymptotic" R region is consistent with our data, suggesting a rather large ultra violet cut-off on inverse wavelengths in effective string models, $r_0^{-1} > 1.3$ GeV.

In the range $r \geq .75$ fm, we observe a remarkable stability of long flux tubes in the

---

[24] It goes without saying that an approach based on the measurement of Polyakov lines would neither be amenable to such an improvement programme towards "early T asymptotics" nor would it be safe from L_S-periodic effects from mirror sources.

sense that field accretion exclusively occurs in the center plane of the tube, as the sources are further pulled apart. This is another important quantitative support for the flux tube picture. The issue of establishing a definite tube profile (like Gaussian transverse shape) will remain a rather elusive subject for any numerical approach like ours.

The present research can readily be generalized to the situation of more than two static sources, like three quark sources in $SU(3)$ [35] or the case of "nuclear chemistry", with two quark-antiquark pairs in $SU(2)$. The latter has been studied recently by Green and coworkers [36] in the context of hadronic potentials, while the former will help to answer interesting questions related to the three-body character of colour forces in the proton. Work along this line is in progress.

The methods described here should also be useful in the quantitative studies of the confinement mechanism in the maximal Abelian gauge [13, 14, 15].

During completion of this work, we have received a preprint of Haymaker et al. [32]. They work at β-values up to 2.5 and refrain from applying ground state enhancement techniques. Instead, they attempt T-extrapolations on derived flux tube properties. This enforces a smaller R range and implies less control on systematic effects.

Acknowledgements. G.B. thanks R. Sommer and B. Bunk for inspiring and helpful discussions. M. Lüscher is acknowledged for suggesting the center group idea. We are grateful to the Deutsche Forschungsgemeinschaft for providing the Datavault to our 256 MByte CM-2 parallel computer, on which the 16^4 and 32^4 lattices were computed. Moreover, we thank Prof. Rollnik and Dr. Völpel for their support to simulate the $48^3 \times 64$ lattice on the 2 GByte CM-5 at the Gesellschaft für Mathematik und Datenverarbeitung within the HLRZ setup.

Appendix

A Weak coupling expansion of field distributions

In this appendix, we recall the one gluon exchange approximation to the lattice potential and compute the leading order perturbative contribution to the electric energy distribution.

With the lattice gluon propagator in Feynman-t'Hooft gauge,

$$a,\mu \xrightarrow{k} b,\nu \quad : \quad \frac{\delta_{ab}\delta_{\mu\nu}}{\sum_\mu \bar{k}_\mu^2} \quad , \quad \bar{k}_\mu = 2\sin k_\mu/2 \quad , \tag{74}$$

a weak coupling expansion of the Wilson loop yields

$$W(\mathbf{R},T) = 1 + C_F g^2 \sum_{\tau,\tau'=0}^{T} \left(G(\mathbf{R},\tau'-\tau) - G(\mathbf{0},\tau'-\tau)\right) \quad , \tag{75}$$

where just terms, extensive in T, have been kept and the leading term *one* is the expectation value of the loop with the interaction switched off. Note, that we have neglected the zero momentum contribution in the calculation that is suppressed by a factor $1/(L_S^3 L_T)$. The colour factor C_F can be calculated by contracting the colour indices of the $SU(N)$ generators T_a $(a = 1,\ldots,N^2-1)$:

$$C_F = \frac{1}{N}\mathrm{Tr}\{T_a T_b\}\delta_{ab} = \frac{N^2-1}{2N} \quad . \tag{76}$$

Fourier transforming Eq. 74 yields

$$\begin{aligned} G(n) &= \sum_{k\neq 0} \frac{e^{ikn}}{\bar{k}_\mu^2} \quad , \\ k_i &= \frac{2\pi}{L_S} m_i \quad , \qquad m_i = -\frac{L_S}{2}+1,\ldots,\frac{L_S}{2} \quad , \\ k_4 &= \frac{2\pi}{L_T} m_4 \quad , \qquad m_4 = -\frac{L_T}{2}+1,\ldots,\frac{L_T}{2} \end{aligned} \tag{77}$$

for the real space gluon propagator on a finite lattice. With

$$G_L(\mathbf{R}) = \sum_\tau G(\mathbf{R},\tau) = \sum_{\mathbf{k}\neq\mathbf{0}} \frac{e^{i\mathbf{kR}}}{\sum_i \bar{k}_i^2} \tag{78}$$

and $V(\mathbf{R}) = -\lim_{T\to\infty} \ln\left(W(\mathbf{R},T)\right)/T$ one obtains

$$V(\mathbf{R}) = -C_F g^2 \left(G_L(\mathbf{R}) - G_L(\mathbf{0})\right) \quad . \tag{79}$$

By construction, the weak coupling expansion of the quantity (Eq. 23),

$$\langle\Box\rangle_{\mathcal{W}} = \langle\Box\rangle\left(\frac{\langle\Box\mathcal{W}\rangle}{\langle\Box\rangle\langle\mathcal{W}\rangle} - 1\right) \quad , \tag{80}$$

involves only interactions between the plaquette and the Wilson loop. All self-interactions of the plaquette and Wilson loop are cancelled by the denominator.

An expansion of the plaquette yields

$$\langle\Box\rangle = 1 - c_1 g^2 + \cdots \tag{81}$$

with $c_1 = 2C_f g^2(G(0) - G(1)) = C_F g^2/4$ on symmetric lattices. If we are interested in the leading order behaviour only, the plaquette can be approximated by *one*. However, at realistic values of the coupling higher order corrections are large. At $\beta = 2.5$ we find for example $\langle\Box\rangle = .65198$. This observation inspired Parisi to formulate a programme of mean field improved lattice operators [37]. The idea is to split every lattice operator into a part that corresponds to (discretization dependent) fluctuations on the ultra violet lattice scale and a *physical* infra red part.

More recently, the deviations of lattice results from perturbative expansions in terms of the bare lattice coupling parameter have been explained as being due to large contributions from tadpole diagrams [38]. This circumstance has revived the interest in mean field or tadpole improved lattice perturbation theory and operators. The hope is to suppress ultra violet contaminations by dividing every link in a given lattice operator by its Monte Carlo mean field value u_0. This is supposed to procure early asymptotic scaling and reliable perturbation theory predictions.

A popular choice of u_0 is the fourth root of the average plaquette. Following this procedure, we should divide the expression on the r.h.s. of Eq. 80 by the average plaquette. However, in the end, we are interested in the combination $\beta\langle\Box\rangle_{\mathcal{W}}$ only. Since the plaquette in the action $S_W - \beta U$ has also to be divided by its mean field value, β is replaced by a mean field coupling $\beta_{MF} = \beta\langle\Box\rangle$. Performing both replacements, the $\langle\Box\rangle$ contributions cancel. In this spirit, the definition of action and energy densities in Section 2.4 represents already in itself a tadpole improved definition. Keeping in mind that in the last step our operator will be multiplied by β, it is justified to neglect the multiplicative $\langle\Box\rangle$ factor in Eq. 80 even in a region where g^2 depending deviations from *one* are not small.

The two loops being disconnected in colour space, only singlets can be exchanged. Thus, we expect an exchange of two gluons as the leading order contribution. Technically, this can be seen as follows: for computation of the product of two (real) traces, both possible relative orientations of the Wilson loop and the plaquette have to be averaged over. Thus, exchanges of single (bare or dressed) gluons cancel. The same holds for a triple gluon vertex that can only be attached with two legs to one loop and with one leg to the other. Due to the Lorentz structure of the propagator Eq. 74, magnetic plaquettes cannot interact by a direct exchange of gluons with the timelike links of the Wilson loop.

The colour factor of the two gluon exchange between the disconnected loops turns out to be:

$$\frac{1}{N}\mathrm{Tr}\{T_aT_b\}\frac{1}{N}\mathrm{Tr}\{T_cT_d\}\delta_{ac}\delta_{bd} = \frac{1}{2N}\frac{1}{N}\mathrm{Tr}\{T_aT_b\}\delta_{ab} = \frac{C_F}{2N} \tag{82}$$

By squaring the one-gluon exchange contribution, dividing the expression by a factor *two* to avoid an overcounting of gluon exchanges, and performing the T integration, we obtain (Again, only terms extensive in T have been kept.):

$$\begin{aligned}\langle U(\mathbf{n})_{i4}\rangle_{\mathcal{W}} &= y_i(\mathbf{n}) \\ &= \frac{C_F g^4}{4N}\left(G_L(\mathbf{n}-\mathbf{r}_1+\mathbf{e}_i) - G_L(\mathbf{n}-\mathbf{r}_1)\right. \\ &\qquad \left. - G_L(\mathbf{n}-\mathbf{r}_2+\mathbf{e}_i) + G_L(\mathbf{n}-\mathbf{r}_2)\right)^2 \quad ,\end{aligned} \tag{83}$$

where the sources are placed at the positions $\mathbf{r}_1 = \frac{R}{2}\mathbf{e}_1$. and $\mathbf{r}_2 = -\frac{R}{2}\mathbf{e}_1$.

After averaging over the two plaquettes used for construction of the electric field operator and multiplying by $2\beta/a^4$, we end up with

$$a^4\langle E_i^2(\mathbf{n})\rangle_{|0,R\rangle-|0\rangle} = g^2 C_F \frac{y_i(\mathbf{n}) + y_i(\mathbf{n}-\mathbf{e}_i)}{2} \tag{84}$$

while

$$a^4\langle B_i^2(\mathbf{n})\rangle_{|0,R\rangle-|0\rangle} = \mathcal{O}(g^4) \quad . \tag{85}$$

Many of the higher order diagrams contribute to $\mathcal{B}$ as well as to $\mathcal{E}$. Thus, we would expect a partial cancellation of higher order effects in the energy density

$$\epsilon_R(\mathbf{n}) = \frac{\mathcal{E}_R(\mathbf{n}) - \mathcal{B}_R(\mathbf{n})}{2} \quad . \tag{86}$$

From

$$\sum_{\mathbf{n},i} y_i(\mathbf{n}) = 2\left(G_L(0) - G_L(R)\right) \quad , \tag{87}$$

we obtain

$$a^4\sum_{\mathbf{n}} \epsilon_R(\mathbf{n}) = g^2 C_F (G_L(0) - G_L(R)) + \mathcal{O}(g^4) \approx V(R) \quad . \tag{88}$$

Note, that to order g^2 the action density equals the energy density. However, the action density is expected to deviate much more from the leading order perturbative expectation since higher order electric and magnetic contributions are added and no cancellations of diagrams occur.

Perturbation theory yields (up to a divergent self-energy part)

$$v(r) = -C_F g^2 \frac{1}{4\pi r} \tag{89}$$

for the continuum potential. The associated electric field is given (up to a colour factor) by $g^{-1}\nabla\left(v(\mathbf{x}+r/2\mathbf{e}_1)-v(\mathbf{x}-r/2\mathbf{e}_1)\right)$. In the continuum limit the differences in Eq. 83 will be replaced by derivatives, yielding exactly this expression. After squaring and expressing the result in lattice units, one obtains:

$$\epsilon_R^{(c)}(\mathbf{n}) = g^2 C_F \frac{1}{(4\pi)^2}\sum_i \left(\frac{n_i-\delta_{i1}R/2}{|\mathbf{n}-\mathbf{e}_1R/2|^3}-\frac{n_i+\delta_{i1}R/2}{|\mathbf{n}+\mathbf{e}_1R/2|^3}\right)^2+\cdots \tag{90}$$

which is just the continuum limit of Eq. 84.

B Action sum rule

In order to derive the action sum rule we start from the definition ($\mathcal{W}=W(R,T)$, Dirac indices and spatial position are suppressed):

$$\langle\Box\rangle_{\mathcal{W},2}=\frac{1}{T}\sum_{\tau=0}^{L_T-1}\left(\frac{\langle\Box(\tau)\mathcal{W}\rangle}{\langle\mathcal{W}\rangle}-\langle\Box\rangle\right)=\frac{2}{T}\sum_{S=0}^{L_T/2-1}\langle\Box(S)\rangle_{\mathcal{W}} \quad . \tag{91}$$

In Eq. 24, the spectral decomposition of the argument of the sum for $0\le S<T/2$ has been carried out. For the plaquette position outside the loop, i.e. $S\ge T/2$, we obtain:

$$\langle\Box(S)\rangle_{\mathcal{W}}=\text{const.}\times e^{-E_1(L_T-T)/2}\cosh\left(E_1(L_T/2-S)\right)+\cdots \quad . \tag{92}$$

The signal is suppressed with the temporal distance of the plaquette insertions from the Wilson loop, $S-T/2$, times the mass gap, $E_1=m_{A_1^+}a\approx 3\sqrt{K}$, [39] in the exponent.

After summing over all S, we obtain:

$$\begin{aligned}\langle\Box\rangle_{\mathcal{W},2} &= \langle\Box\rangle_{|0,R\rangle-|0\rangle}\\ &+ \frac{b}{T}+\frac{|d_1|^2}{|d_0^2|}e^{-\Delta VT}+\mathcal{O}\left(\frac{e^{-\Delta VT}}{T}\right) \quad .\end{aligned} \tag{93}$$

We have made use of the fact that the off-diagonal (i.e. S dependent) pollutions, inside and outside the loop are incomplete geometric series. The summation gives, apart from the constant parts, only multiplicative $1-e^{-n\Delta V(T+1)}$ or $1-e^{-nE_1(L_T-T+1)}$ factors. The constant $b_{\mu\nu}(\mathbf{n})$ is the sum of all off-diagonal coefficients from the expansions Eq. 24 and Eq. 92 of $\langle\Box\rangle_{\mathcal{W}}$, weighted by corresponding coefficients $(1-e^{-\Delta V_i})^{-1}$ or $(1-e^{-E_i})^{-1}$.

Together with

$$\langle\mathcal{W}\rangle=\int\mathcal{D}U\,\mathcal{W}e^{\beta U} \quad , \quad U=\sum_{n,\mu>\nu}U_{\mu\nu}(n) \quad , \tag{94}$$

and the decomposition of the Wilson loop (Eq. 4) we obtain from Eq. 93:

$$\begin{aligned}\sum_{\mathbf{n},\mu>\nu}\langle U_{\mu\nu}(\mathbf{n})\rangle_{\mathcal{W},2} &= \frac{1}{T}\left(\frac{\langle U\mathcal{W}\rangle}{\langle\mathcal{W}\rangle}-\langle U\rangle\right)\\ &= \frac{1}{T}\frac{\partial}{\partial\beta}\ln\langle\mathcal{W}\rangle \qquad (95)\\ &= \frac{1}{T}\frac{\partial\ln|d_0|^2}{\partial\beta}-\frac{\partial V}{\partial\beta}-\frac{\partial\Delta V}{\partial\beta}\frac{|d_1|^2}{|d_0|^2}e^{-\Delta VT}-\cdots\end{aligned}$$

Note, that the equalities are exact! Thus, in the expansion of the derivative of the Wilson loop the same terms appear as in Eq. 93.

A comparison of the $1/T$ coefficients between the above equation and b of Eq. 93 yields

$$B=\sum_{\mathbf{n},\mu>\nu}b_{\mu\nu}(\mathbf{n})=\frac{\partial\ln|d_0|^2}{\partial\beta}\quad . \qquad (96)$$

From the estimate for ground state overlaps of unsmeared operators Eq. 18 we obtain

$$B=-R\frac{\partial V_0}{\partial\beta}\approx\beta^{-1}V_0R \qquad (97)$$

for large R and weak coupling. The monotonous increase of the ground state overlap at fixed R with β is confirmed in the present simulation. Therefore, B is positive. For smeared operators, V_0 is replaced by some constant f that is small compared to all R^{-1}, such that the exponential can be expanded and the ground state overlaps $|d_0(R)|^2$ exhibit the linear behaviour of Fig. 2. f is expected to be proportional to g^2 to the lowest order such that $B\approx\beta^{-1}fR$. Under the assumption that d_1 dominates other excited state overlaps, we obtain $|d_1(R)|^2\approx fR$. Eq. 91 can also serve as a definition for colour field measurement operators. However, we have preferred to use $\langle\Box\rangle_{\mathcal{W}}$ instead, due to the better asymptotic behaviour: excited states are suppressed by factors proportional to $\sqrt{R}e^{-\Delta VT/2}\approx\sqrt{R}e^{-\frac{\pi}{R}T}$ instead of R/T only.

From Eqs. 20, 21, 23, 27 and 28, one obtains:

$$\sum_{\mathbf{n},\mu>\nu}\langle U_{\mu\nu}(\mathbf{n})\rangle_{\mathcal{W},2}\overset{T\to\infty}{\longrightarrow}\frac{a^4}{\beta}\sum_{\mathbf{n}}\frac{1}{2}\left(\mathcal{E}(\mathbf{n})-\mathcal{B}(\mathbf{n})\right)=\frac{a^4}{\beta}\sum_{\mathbf{n}}\sigma_R(\mathbf{n})\quad . \qquad (98)$$

By carefully comparing the coefficients of the expansions one finds many (exact) "sum rules". In the following we list three such examples.

$$\begin{aligned}\sum_{\mathbf{n}}a^3\sigma_R(\mathbf{n}) &= -\frac{\beta}{a}\frac{\partial V}{\partial\beta}\quad , &(99)\\ \sum_{\mathbf{n}}a^3\left(\sigma_R'(\mathbf{n})-\sigma_R(\mathbf{n})\right) &= -\frac{\beta}{a}\frac{\partial\Delta V}{\partial\beta}\quad , &(100)\\ \sum_{\mathbf{n}}a^3\sigma_{A_1^+}(\mathbf{n}) &= -\frac{\beta}{a}\frac{\partial E_1}{\partial\beta}\quad . &(101)\end{aligned}$$

σ'_R denotes the action density distribution of the first excited $Q\bar{Q}$ state without angular momentum, $\sigma_{A_1^+}$ is the action density distribution in presence of the lightest glueball state.

The ground state potential consists of a constant physical part $v(R)$ and a self energy contribution V_0 which diverges in the continuum limit:

$$V(R) = av(R) + V_0 \tag{102}$$

By using this decomposition, we obtain from Eq. 99 the action sum rule

$$\sum_{\mathbf{n}} a^3 \sigma_R(\mathbf{n}) = -\frac{\partial \ln a}{\partial \ln \beta} v(R) - \frac{1}{a}\frac{\partial V_0}{\partial \ln \beta} \quad . \tag{103}$$

C Energy sum rule

The derivation of the energy sum rule, though the more intuitive one, turns out to be more complicated. We start from the decomposition of the Wilson action into a spatial and a temporal part

$$S_W = -\beta_t U_t - \beta_s U_s \quad . \tag{104}$$

In the following, the spatial and temporal lattice spacings will be called a_s and a_t, respectively. The asymmetry is defined by $\xi = a_s/a_t$. Following the steps of the previous section, one finds:

$$\frac{a_s^4}{2\beta}\sum_{\mathbf{n}} \mathcal{E}_R(\mathbf{n}) \quad \overset{T\to\infty}{\longleftarrow} \quad \xi \sum_{\mathbf{n},i} \langle U_{i4}(\mathbf{n})\rangle_{\mathcal{W},2} = \frac{\xi}{T}\frac{\partial}{\partial \beta_t}\ln\langle\mathcal{W}\rangle \quad , \tag{105}$$

$$\frac{a_s^4}{2\beta}\sum_{\mathbf{n}} \mathcal{B}_R(\mathbf{n}) \quad \overset{T\to\infty}{\longleftarrow} \quad -\sum_{\mathbf{n},i>j} \langle U_{ij}(\mathbf{n})\rangle_{\mathcal{W},2} = -\frac{1}{T}\frac{\partial}{\partial \beta_s}\ln\langle\mathcal{W}\rangle \quad . \tag{106}$$

A weak coupling expansion [40] relates the anisotropic lattice couplings to the isotropic coupling $\beta(a_s)$:

$$\beta_s \xi = \beta + 2N c_s(\xi) + \mathcal{O}(\beta^{-1}) \quad , \tag{107}$$

$$\beta_t \xi = \beta + 2N c_t(\xi) + \mathcal{O}(\beta^{-1}) \quad . \tag{108}$$

The coefficients fulfil the relations:

$$c_s(1) = c_t(1) = 0 \quad , \quad c'_s(1) + c'_t(1) = b_0 = \frac{11N}{48\pi^2} \quad . \tag{109}$$

The derivatives of the coefficients have been calculated by Karsch in Ref. [40]. For $SU(2)$ the result is

$$c'_s = c'_s(1) = .11403\ldots \quad , \quad c'_t = c'_t(1) = -.06759\ldots \quad . \tag{110}$$

After expressing the derivatives in respect to the asymmetric couplings by derivatives in respect to β and ξ and taking $\xi = 1$, we end up with:

$$a^4 \sum_{\mathbf{n}} \mathcal{E}_R(\mathbf{n}) = -\frac{\partial V}{\partial \ln \beta}\left(1 - \frac{N}{\beta} b_0\right) + V\left(1 - \frac{N}{\beta}(c'_t - c'_s)\right) \tag{111}$$

$$a^4 \sum_{\mathbf{n}} \mathcal{B}_R(\mathbf{n}) = \frac{\partial V}{\partial \ln \beta}\left(1 + \frac{N}{\beta} b_0\right) + V\left(1 - \frac{N}{\beta}(c'_t - c'_s)\right) \tag{112}$$

Subtracting both expression yields the (exact) action sum rule Eq. 99.

Adding Eqs. 111 and 112 and dividing by a factor *two* yields the energy sum rule

$$\sum_{\mathbf{n}} a^3 \epsilon_R(\mathbf{n}) = \frac{1}{a}\left(V\left(1 - \frac{N}{\beta}(c'_t - c'_s)\right) + \frac{\partial V}{\partial \ln \beta}\frac{N}{\beta} b_0 + \cdots\right) \tag{113}$$

$$\begin{aligned} &= \left(v + \frac{V_0}{a}\right)\left(1 - \frac{N}{\beta}(c'_t - c'_s)\right) \\ &+ \left(v\frac{\partial \ln a}{\partial \ln \beta} + \frac{1}{a}\frac{\partial V_0}{\partial \ln \beta}\right)\frac{N}{\beta} b_0 + \cdots \end{aligned} \tag{114}$$

The energy sum rule is not exact due to the perturbative origin of the relation between the symmetric and asymmetric couplings (Eqs. 107, 108). Of course, it would be preferable to measure the corresponding derivatives of $\ln a$ directly on the lattice instead.

Note that the coefficient of the last term in Eq. 114 is identical to the action sum Eq. 103. The factor $\partial \ln a / \partial \ln \beta$ appearing in front of v within this term carries an anomalous dimension (as the action does), cancelling a β^{-1} factor. Thus, an additional factor $-v/4$ seems to survive the continuum limit $a \to 0$. Its origin is an incomplete resummation of the series: the non-perturbatively determined coefficients contribute to all orders in β^{-1}. The order β^{-1} term yielding the above $-v/4$ contribution has to be cancelled by other anomalous terms appearing in higher orders of the expansion. However, if consistently cutting the expansion at order β^{-2} by expanding the potential perturbatively, the coefficient *one* is reproduced in accord to the expected continuum limit.

D Finite Size Corrections

In this appendix, we elaborate details on the computation of finite size corrections on the action/energy density distributions within the center plane. These FSE are mainly due to the periodicity of the measurement operator,

$$O_R(0, n_2, n_3) = O_R(0, L_S - n_2, L_S - n_3) \quad , \tag{115}$$

at a given $Q\bar{Q}$ separation, $\mathbf{R} = R\mathbf{e}_1$. This mirror source effect should not be confused with contributions from the replacement $R \to R \pm nL_S$ which are negligible (as shown in Section 4.2.3). We also neglect effects from mirror sources along the $Q\bar{Q}$ axis which are almost completely screened from the center plane since the colour field densities fall off at least as fast as $(|n_1| - R/2)^{-4}$ into the longitudinal direction. The effect from mirror copies placed along the transverse directions can be substantial (depending on the ratio δ/L_S).

We perform our calculations for two models, namely a dipole transverse shape,

$$f_d(x_\perp;\infty) = \frac{c}{\pi}\frac{\delta^2}{\left(\delta^2 + x_\perp^2\right)^3} \quad , \tag{116}$$

and a Gaussian shape

$$f_g(x_\perp;\infty) = \frac{c}{2\pi\delta^4}\exp\left(-\frac{x_\perp^2}{\delta^2}\right) \quad . \tag{117}$$

$f_d(x_\perp;\infty)$ and $f_g(x_\perp;\infty)$ are the corresponding (infinite volume) center plane energy/action density distributions.

As argued above it is justified to neglect interactions between different pairs of mirror sources. We also assume that the chromo electric and magnetic fields on the finite volume can be obtained by superimposing the (infinite volume) fields of all (pairs of) mirror sources. Note, that we have to add the fields rather than the action and energy densities themselves. From the geometry it is clear that the perpendicular electric and longitudinal magnetic field components vanish in the center plane. Under the assumption that the (perpendicular) magnetic field component is proportional to the (longitudinal) electric component, we find:

$$f(x_2, x_3; L_S) = \left(\sum_{n_2,n_3} g\left(x_2 + n_2 L_S, x_3 + n_3 L_S\right)\right)^2 \tag{118}$$

with $g(x_2, x_3) = g(x_\perp) = \sqrt{f(x_\perp;\infty)}$. The integrated area can be computed in the following way:

$$\begin{aligned} A(L_S) &= \int_0^{L_S} dx_2 dx_3\, f(x_2, x_3; L_S) \qquad (119)\\ &= \sum_{n_2 n_3}\sum_{m_2 m_3}\int_{m_2 L_S}^{(m_2+1)L_S} dx_2 \int_{m_3 L_S}^{(m_3+1)L_S} dx_3\, g\left(x_\perp\right) g\left(x_2 + n_2 L_S, x_3 + n_3 L_S\right)\\ &= \sum_{n_2 n_3}\int d^2x_\perp\, g\left(x_2 - n_2 L_S/2, x_3 - n_3 L_S/2\right)\\ &\qquad\qquad \times g\left(x_2 + n_2 L_S/2, x_3 + n_3 L_S/2\right) \quad . \qquad (120) \end{aligned}$$

In case of a dipole field with (infinite volume) r.m.s. width, δ, we have

$$g_d(x_\perp) \propto \left(\delta^2 + x_\perp^2\right)^{-3/2} \tag{121}$$

and obtain for the area,

$$A(L_S) \propto \sum_{n_2 n_3} \int_0^{2\pi} d\phi \int_0^{\infty} dr\, r \left(d^2(n_2, n_3) + r^2 \left(1 - L_S^2 (n_2 \cos\phi + n_3 \sin\phi)^2 \right) \right)^{-3/2} \tag{122}$$

with

$$d^2(n_2, n_3) = \delta^2 + \frac{L_S^2}{4} (n_2^2 + n_3^2) \quad . \tag{123}$$

After performing the radial integration, we arrive at:

$$\begin{aligned} A(L_S) &\propto \sum_{n_2 n_3} \frac{1}{d^2} \int_0^{2\pi} d\phi \, \frac{1}{4d^2 - L_S^2 (n_2 \cos\phi + n_3 \sin\phi)^2} && (124) \\ &= \frac{\pi}{2} \sum_{n_2 n_3} \frac{1}{d^3 \sqrt{d^2 - L_S^2 (n_2^2 + n_3^2)/4}} && (125) \\ &= A(\infty) \sum_{n_2 n_3} \left(1 + \frac{L_S^2}{4\delta^2} (n_2^2 + n_3^2) \right)^{-3/2} && (126) \end{aligned}$$

with $A(\infty) = c/(2\delta^2)$.

For the Gauss fits we have

$$g_g(x_\perp) \propto \exp\left(-\frac{x_\perp^2}{2\delta^2} \right) \quad . \tag{127}$$

Thus, we end up with

$$\begin{aligned} A(L_S) &= \sum_{n_2 n_3} \int d^2 x_\perp \, \exp\left(-\frac{x_\perp^2}{\delta^2} \right) \exp\left(-\frac{L_S^2}{4\delta^2} (n_1^2 + n_2^2) \right) && (128) \\ &= A(\infty) \sum_{n_2 n_3} \exp\left(-\frac{L_S^2}{4\delta^2} (n_1^2 + n_2^2) \right) \quad . && (129) \end{aligned}$$

In conclusion, the results for both transverse profiles read

$$\begin{aligned} A(L_S) &= A(\infty) \sum_{n_2 n_3} \frac{g_d \left(L_S^2 (n_1^2 + n_2^2)/4 \right)}{g_d(0)} \quad \text{and} && (130) \\ A(L_S) &= A(\infty) \sum_{n_2 n_3} \frac{g_g \left(L_S^2 (n_1^2 + n_2^2)/2 \right)}{g_g(0)} \quad , && (131) \end{aligned}$$

respectively, with $g(x_\perp) = \sqrt{f(x_\perp; \infty)}$ and $A(\infty) = c/(2\delta^2)$. For the typical dipole r.m.s. width $\delta/L_S = 6/32$ we find an increase of the area by 43% due to the finite volume while the corresponding Gaussian result ($\delta/L_S \approx 4/32$) is only affected by 5×10^{-7}. Notice, that the infinite volume δ can be obtained by fits of the form Eq. 118 from finite volume data.

References

[1] G. t'Hooft, in High Energy Physics, Ed. A. Zichichi, Edotorice Compositori, Bologna (1975); S. Mandelstam, Phys. Rep. **23C** (1976) 245.

[2] R. Sommer, Nucl. Phys. **B291** (1987) 673.

[3] R. Sommer, Nucl. Phys. **B306** (1988) 180.

[4] R.W. Haymaker, and J. Wosiek, Phys. Rev. **D43** (1990) 1991; R.W. Haymaker, Y. Peng, V. Singh, and J. Wosiek, Nucl. Phys. [Proc. Suppl.] **B17** (1990) 558.

[5] Y. Peng and R.W. Haymaker, Phys. Rev. **D47** (1993) 5104.

[6] UKQCD collaboration: A.P. Booth et al., Nucl. Phys. **B394** (1993) 509.

[7] G.S. Bali and K. Schilling, Phys. Rev. **D47**(1993)661.

[8] M. Lüscher, K. Symanzik, and P. Weisz, Nucl. Phys. **B173** (1980) 365.

[9] M. Lüscher, Nucl. Phys. **B180** (1981) 317.

[10] S. Perantonis and C. Michael, Nucl. Phys. **B347** (1990) 347.

[11] G.S. Bali, PhD thesis, Wuppertal WUB–DIS 94-01, March 1994.

[12] M. Baker, J.S. Ball, and F. Zachariasen, Phys. Rev. **D34** (1986) 3894; Phys. Rep. **209** (1991) 73; Phys. Rev. **D41** (1990) 2612.

[13] see e.g. the review of T. Suzuki, Nucl. Phys. [Proc. Suppl.]**B30** (1993) 176.

[14] Y. Matsubara, S. Ejiri, and T. Suzuki, Nucl. Phys. [Proc. Suppl.]**B34** (1994) 176; H. Shiba and T. Suzuki, Kanazawa preprint 94-07, April 1994.

[15] J.D. Stack, S.D. Neiman, and R.J. Wensley, Illinois preprint ILL-TH-94, April 1994.

[16] V. Singh, D.A. Brown, and R.W. Haymaker, Phys. Lett. **B306** (1993) 115.

[17] F.R. Brown and T.J. Woch, Phys. Rev. Lett. **28** (1987) 2394; R. Gupta, G.W. Kilcup, A. Patel, S.R. Sharpe, and P. de Forcrand, Mod. Phys. Lett. **A3** (1988) 1367.

[18] K. Fabricius and O. Haan, Phys. Lett. **B143** (1984) 459; A. Kennedy and B. Pendleton, Phys. Lett. **B156** (1985) 393.

[19] G. Parisi, R. Petronzio, and F. Rapuano, Phys. Lett. **128B** (1983) 418.

[20] G.S. Bali and K. Schilling, Phys. Rev. **D46** (1992) 2636.

[21] APE Collaboration: M. Albanese et al., Phys. Lett. **B192** (1987) 163.

[22] A. DiGiacomo, M. Maggiore, and S. Olejnik, Phys. Lett. **B236** (1990) 199; Nucl. Phys. **B347** (1990) 441.

[23] F. Karsch and U. Heller, Nucl. Phys. **B251** (1985) 254.

[24] M. Lüscher, G. Münster, and P. Weiss, Nucl. Phys. **B180** (1981) 1.

[25] C. Michael, Nucl. Phys. **B280** (1987) 13.

[26] G.S. Bali, J. Fingberg, U.M. Heller, F. Karsch, and K. Schilling, Int. Journ. Mod. Phys. **C4** (1993) 1179.

[27] C. Michael, M. Teper, Phys. Lett. **B199** (1987) 95

[28] S. Perantonis, A. Huntley, and C. Michael, Nucl. Phys. **B326** (1989) 544.

[29] G.S. Bali, J. Fingberg, U.M. Heller, F. Karsch, and K. Schilling, Phys. Rev. Lett. **71** (1993) 3059.

[30] F. Karsch and R. Petronzio, Phys. Lett. **139B** (1984) 403.

[31] M. Faber, H. Markum, M. Müller, and S. Olejnik, Phys. Lett. **B247** (1990) 377.

[32] R.W. Haymaker, V. Singh, and Y. Peng, MPI Munich preprint LSUHE–94-159, July 1994.

[33] A. Coste, A. Gonzalez-Arroyo, J. Jurkiewicz, and C.P. Korthals Altes, Nucl. Phys. **B262** (1985) 67.

[34] B. Efron, Ann. Stat. **7** (1979) 1.

[35] R. Sommer and J. Wosiek, Phys. Lett. **149B** (1984) 497; Nucl. Phys. **B267** (1986) 531.

[36] A.M. Green, C. Michael, and J.E. Paton, Nucl. Phys. **A554** (1993) 701; A.M. Green, C. Michael, J.E. Paton, and M.E. Sainio, Int. Journ. Mod. Phys. **E2** (1993) 479; A.M. Green, C. Michael, and M.E. Sainio, Helsinki preprint HU-TFT-94-7 April 1994.

[37] G. Parisi, Proceedings of the XXth International Conference on High Energy Physics 1980, Madison, Eds. L. Durand and L.G. Pondrom, American Institute of Physics, New York (1981) 1531.

[38] G.P. Lepage and P.B. Mackenzie, Phys. Rev. **D48** (1993) 2250.

[39] C. Michael and S.J. Perantonis, J. Phys. **G18** (1992) 1725.

[40] F. Karsch, Nucl. Phys. **B205** (1982) 285.

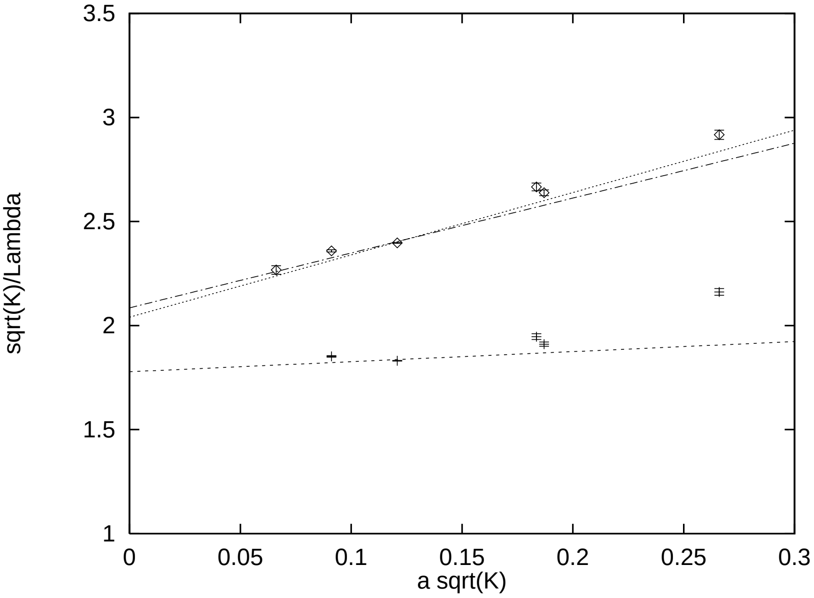

Figure 7: *$\Lambda^{-1}_{\overline{MS}}(a)\sqrt{\kappa}$ versus the lattice spacing $a\sqrt{\kappa}$, both measured in units of the string tension. The estimates for the Λ values have been obtained from the perturbative two loop formula by use of the bare coupling (upper values) and the β_E scheme (lower values). Linear fits to the data are indicated.*

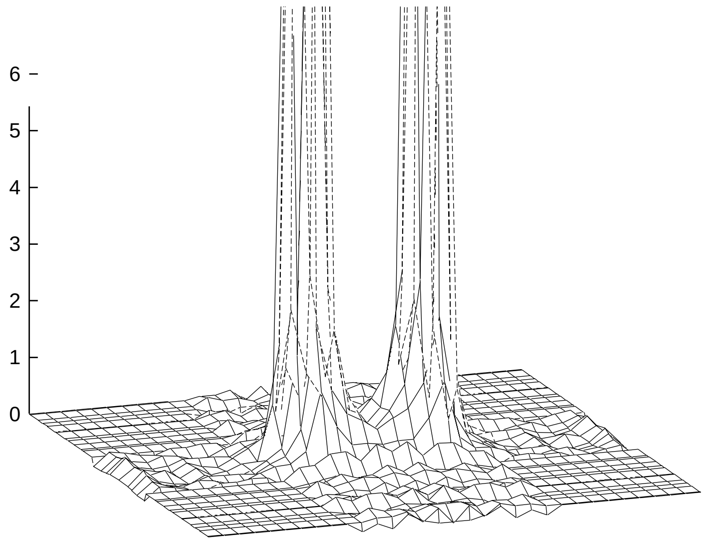

Figure 8: *The energy density distribution at $\beta = 2.5$, $R = 8$ ($r \approx .7$ fm) in units of the string tension.*

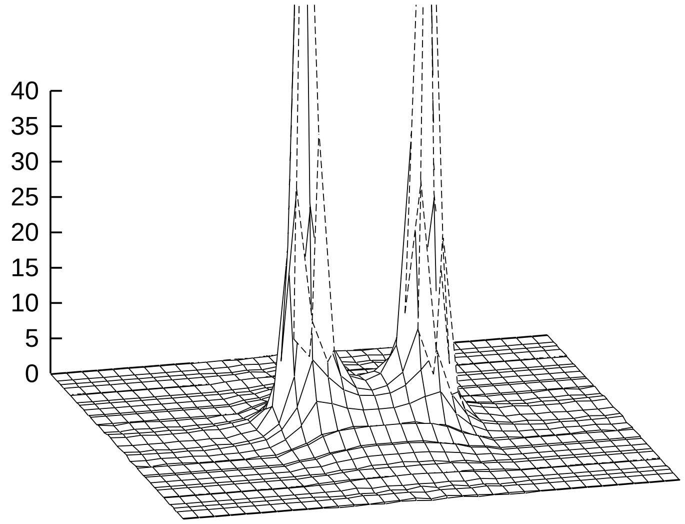

Figure 9: *The action density distribution at $\beta = 2.5$, $R = 8$ ($r \approx .7$ fm) in units of the string tension.*

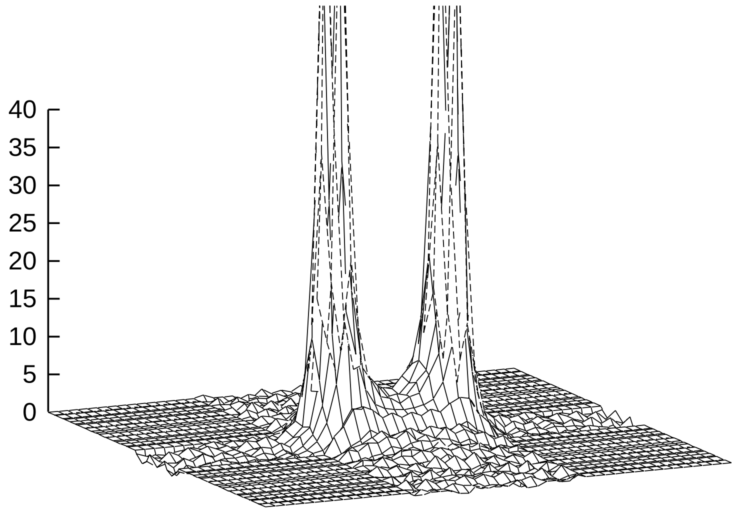

Figure 10: *The action density distribution at $\beta = 2.635$, $R = 12$ ($r \approx .7$ fm) in units of the string tension. Relative to Fig. 9 the vertical axis has been rescaled by the ratio of the corresponding $\tilde{B}(\beta)$ values.*

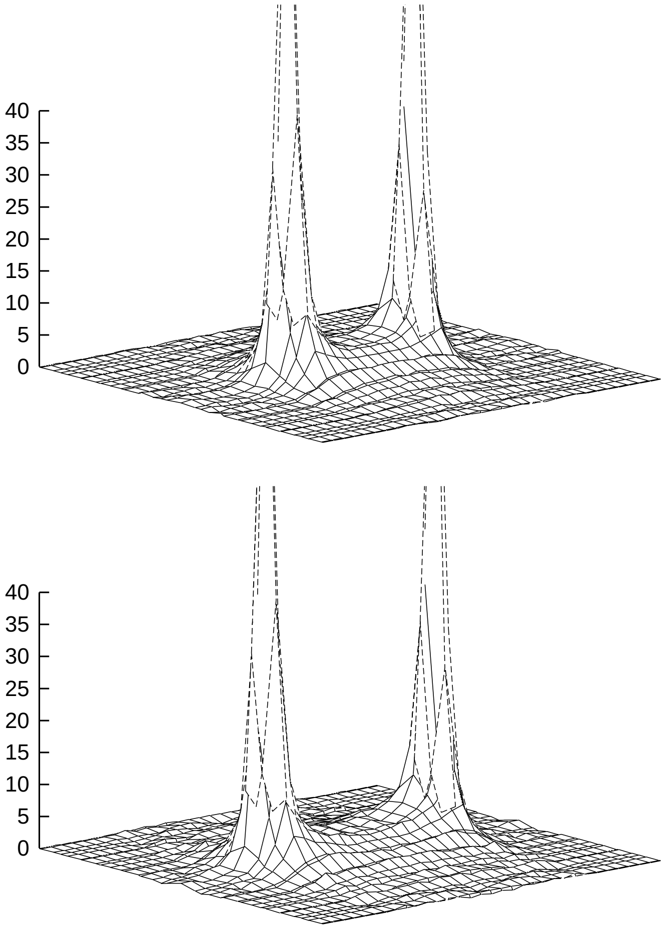

Figure 11: *Same as Fig. 9 for* $R = 12$ *(*$r \approx 1$ *fm) and* $R = 16$ *(*$r \approx 1.35$ *fm).*

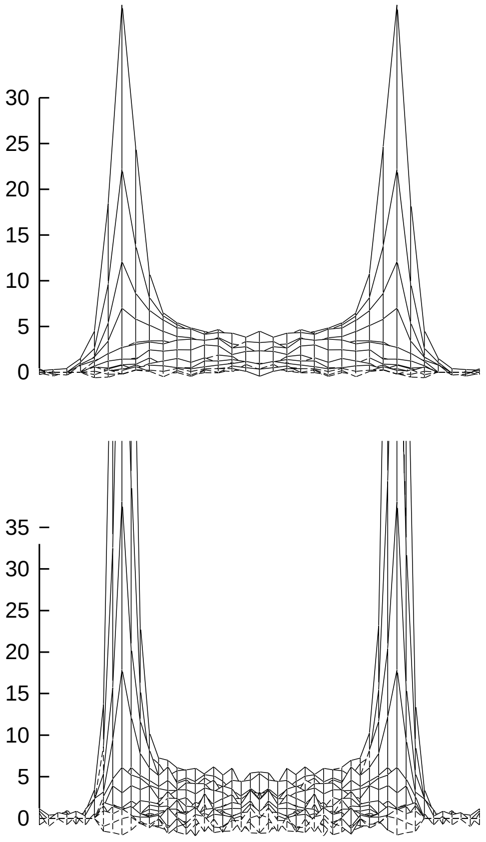

Figure 12: *The action density distributions for quark separations* $R = 20$ *at* $\beta = 2.5$ *and* $R = 30$ *at* $\beta = 2.635$, *corresponding to* $r \approx 1.7$ *fm. The* z *axis of the first plot is expanded by the ratio of the two* $\tilde{B}(\beta)$ *values in respect to the second plot to account for the anomalous dimension.*

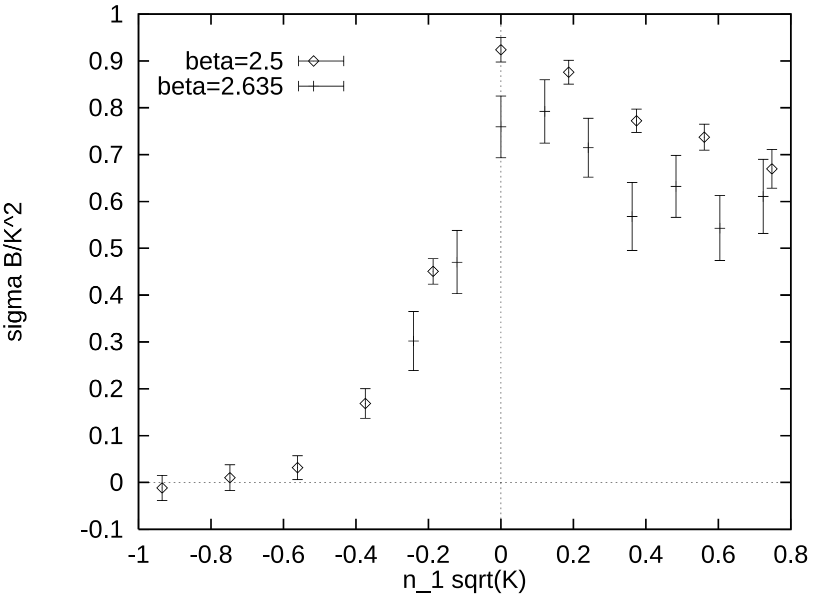

Figure 13: *Comparison of longitudinal action density profiles at* $r = .7$ *fm between the* $\beta = 2.5$ *data (*$R = 8$*) and the* $\beta = 2.635$ *data (*$R = 12$*) at* $n_\perp a = .17$ *fm in units of the string tension. The vertical axis has been multiplied by* $\tilde{B}(\beta)$*. One source is placed at position* $(n_1, n_\perp) = 0$*. The second source is located at* $n_1\sqrt{K} \approx 1.6$ *(outside the visible range).*

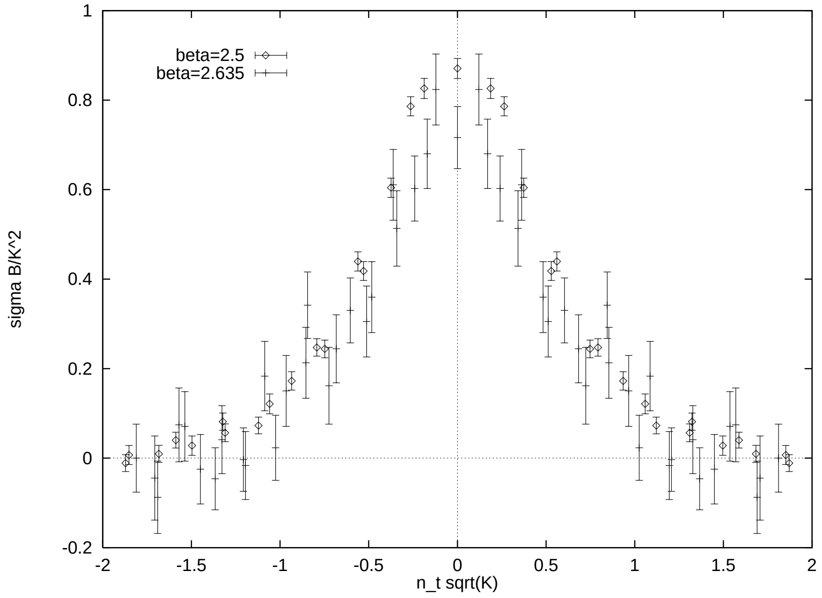

Figure 14: *Comparison of transverse action density profiles at the center plane of two sources, separated by* $r = .7$ *fm between the* $\beta = 2.5$ *data* $(R = 8)$ *and the* $\beta = 2.635$ *data* $(R = 12)$ *in units of the string tension. The vertical axis has been multiplied by* $\tilde{B}(\beta)$.

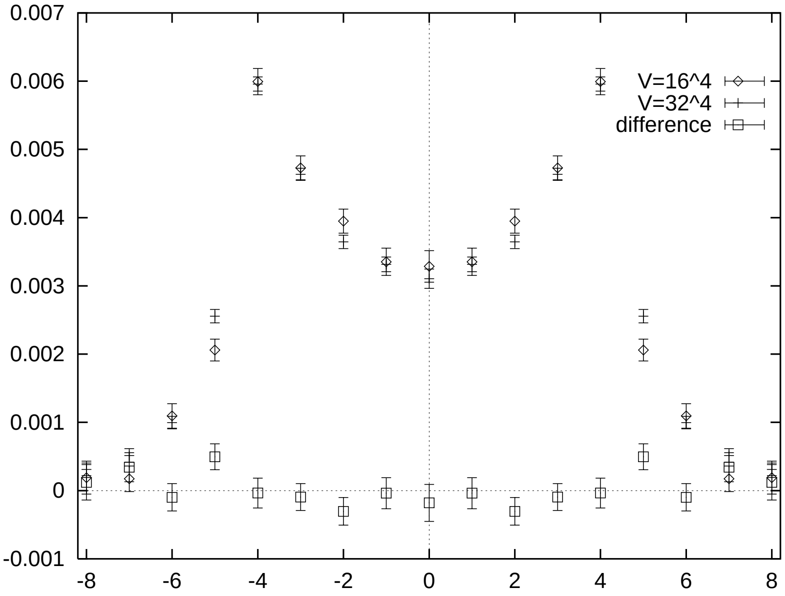

Figure 15: *Differences between the longitudinal action density profiles measured on* 16^4 *and* 32^4 *lattices at* $\beta = 2.5$ *for* $R = 8$ *and* $n_\perp = 2$.

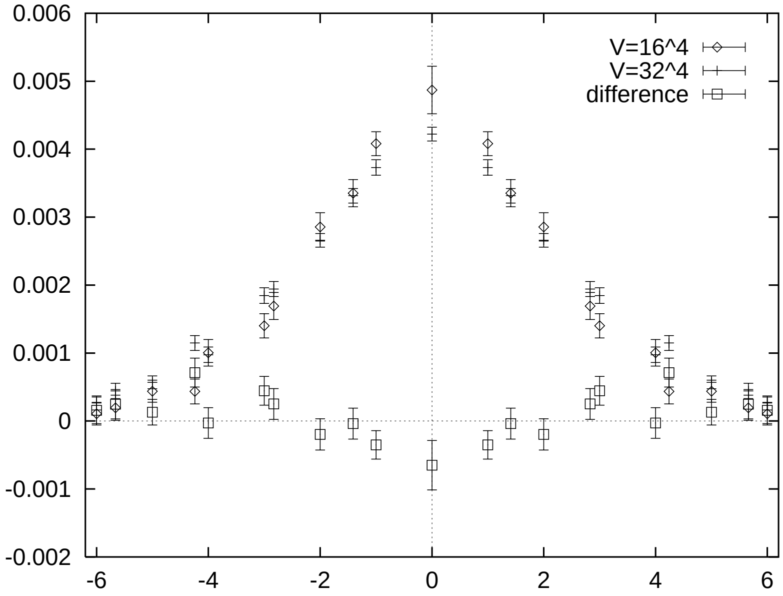

Figure 16: *Differences between the transverse action density profiles measured on* 16^4 *and* 32^4 *lattices at* $\beta = 2.5$ *for* $R = 8$ *and* $n_1 = 0$.

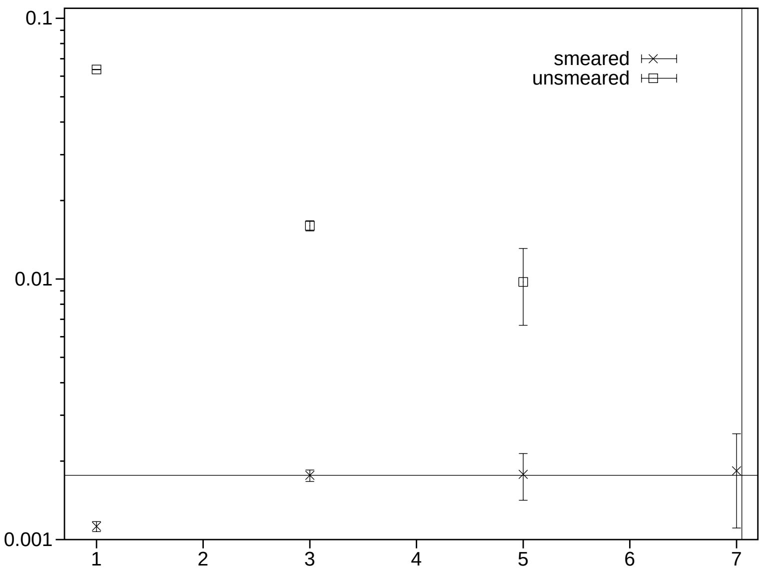

Figure 17: *Comparison between smeared and unsmeared finite T energy density approximants in the center ($n_1 = n_\perp = 0$) between two sources, separated by $R = 4$ at $\beta = 2.74$. The horizontal axis is the time T.*

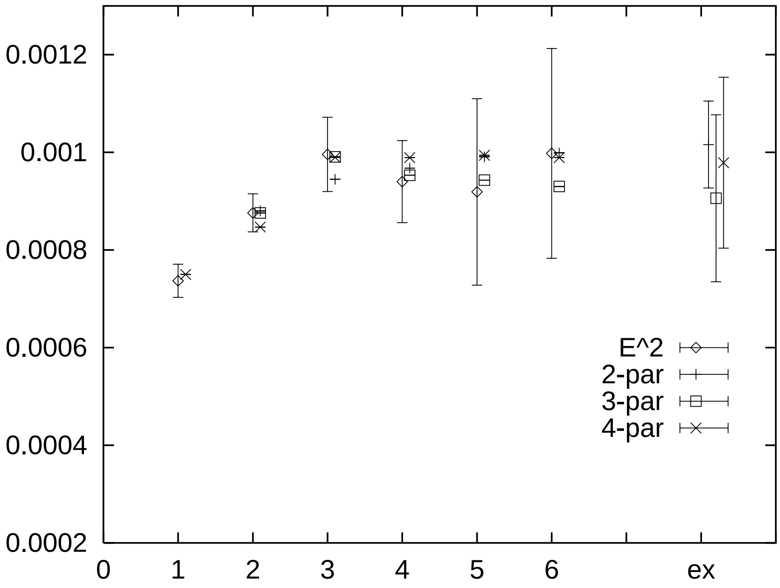

Figure 18: *Finite T approximants to the electric plaquette expectation value* $\mathcal{E}_6(0,3)$ *in presence of two quarks (diamonds), separated by $R = 6$ at $\beta = 2.5$ at the position $n_1 = 0$, $n_\perp = 3$ in lattice units. Two-, three- and four-parameter fits are indicated, together with the corresponding extrapolated asymptotic values (rightmost points with error bars).*

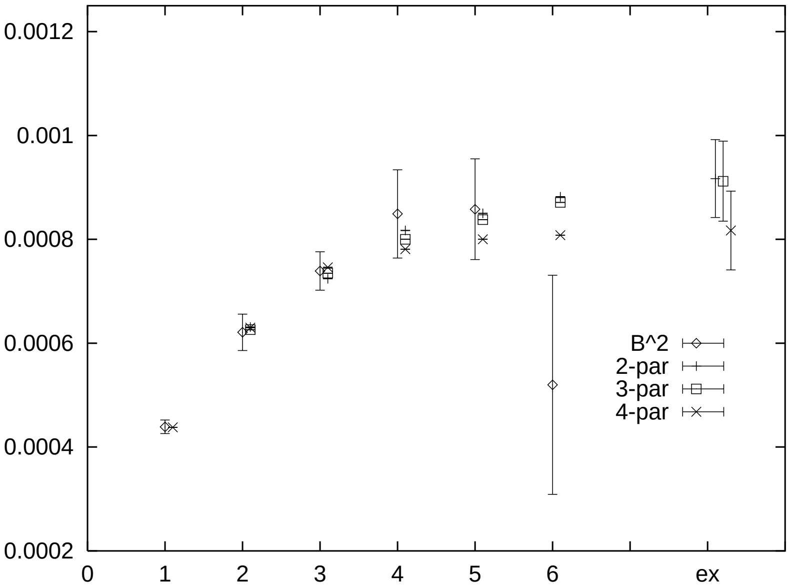

Figure 19: *Same as Fig. 18, but for the magnetic plaquette expectation,* $\mathcal{B}_6(0,3)$.

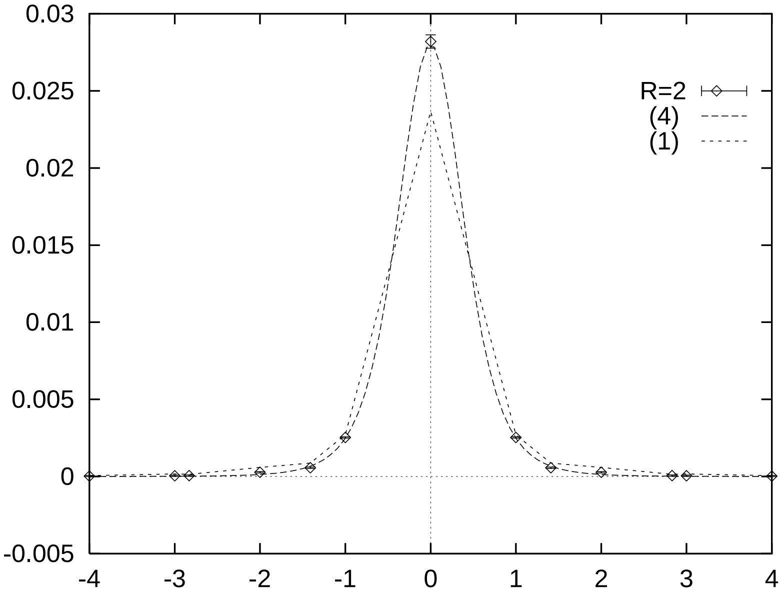

Figure 20: *The central transverse energy density profile at* $R=2$, $\beta=2.5$ *together with fit curves of methods (1) and (4).*

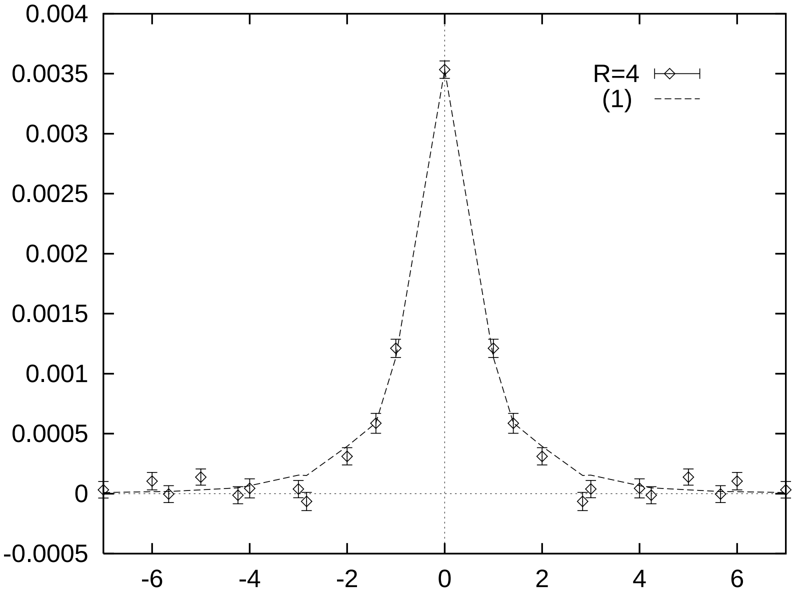

Figure 21: *The central transverse energy density profile at $R = 4$, $\beta = 2.5$ together with a fit to the lattice expression, f_l (method (1)).*

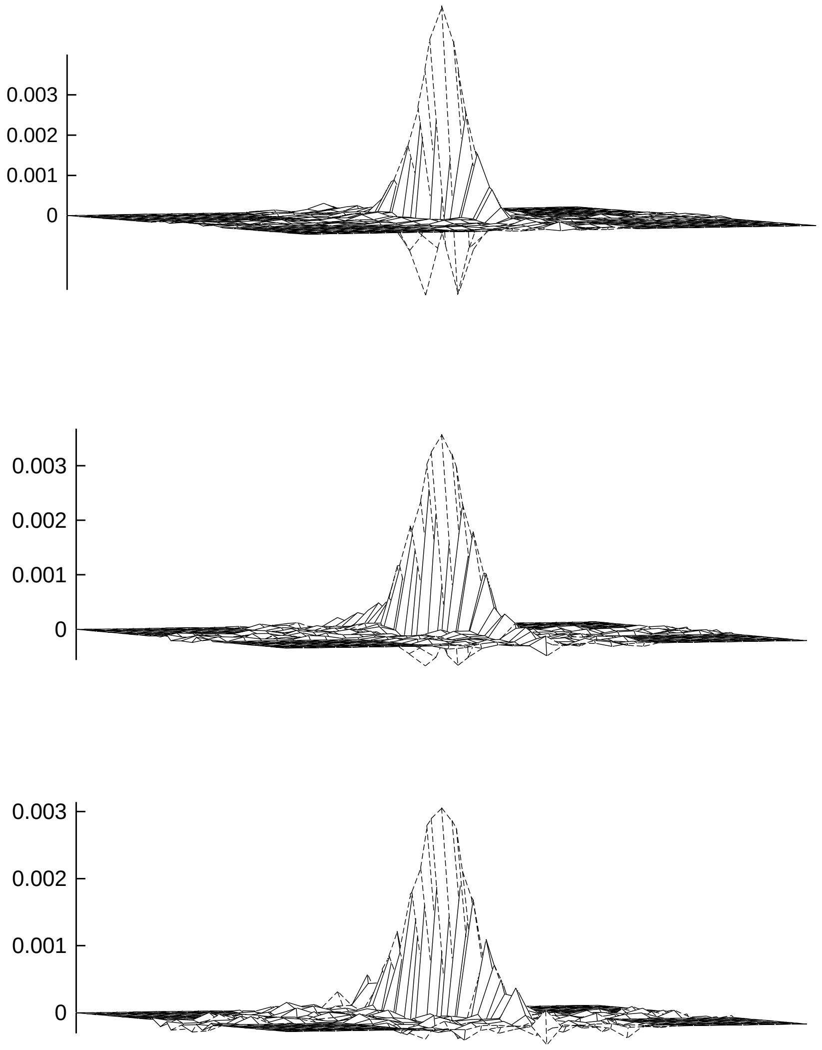

Figure 25: *Differences, $\Delta\sigma_R$, between the action density distributions at R and $R-2$ for $R = 6, 8$, and 10 ($\beta = 2.5$). The sources have been aligned. The labelling corresponds to lattice units.*

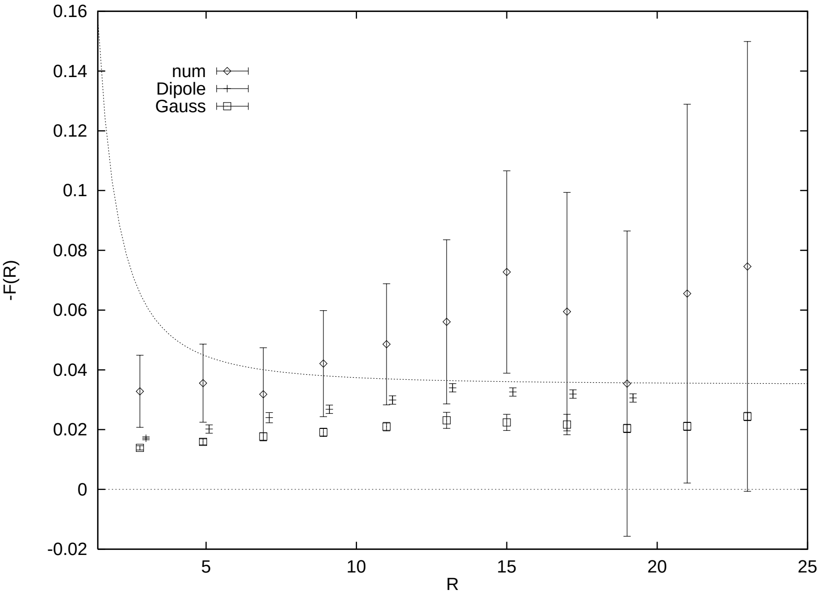

Figure 26: *The $Q\bar{Q}$ force, obtained from the potential at $\beta = 2.5$, compared to the integrated center plane action density, scaled by the anomalous dimension $\tilde{B}$ in lattice units. In addition to the numerically integrated data (num), the dipole and Gauss fit results from Section 5.1 are displayed.*

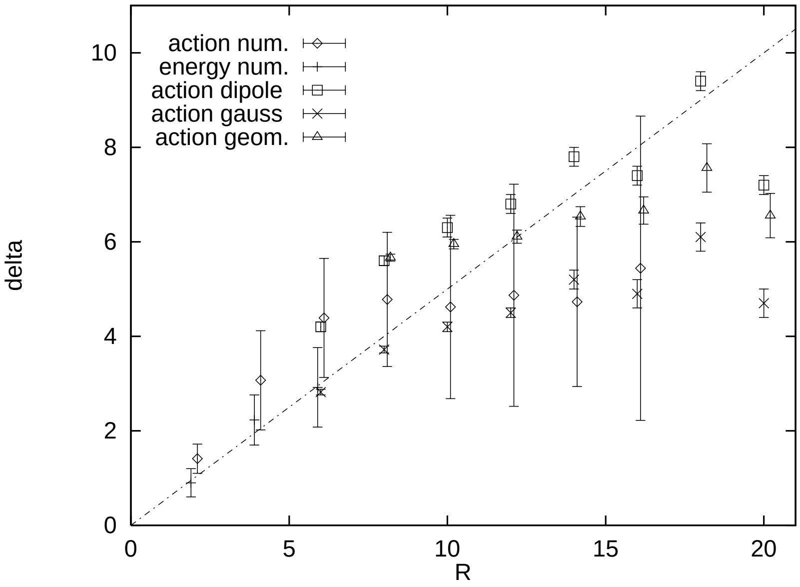

Figure 27: *The width of the flux tube,* δ*, against* R *at* $\beta = 2.5$ *(in lattice units). The dashed line corresponds to* $\delta = R/2$*. In addition to the numerically integrated results from the energy and action density distributions, fit results to the action density from Tab. 10, and results from the geometric method (with* γ*=1) are displayed.*